AD-A071 373 SYSTEMS SCIENCE AND SOFTWARE LA JOLLA CALIF F/G 19/1
CAPRI - A TWO-DIMENSIONAL EULERIAN CODE FOR ANALYZING THE IMPAC--ETC(U)
NOV 78 H E READ, D E WILKINS, J L WADDELL DNA001-76-C-0151
UNCLASSIFIED SSS-R-78-3417 DNA-4751F NL

| OF |
AD
A071373

END
DATE
FILMED
8-79
DDC

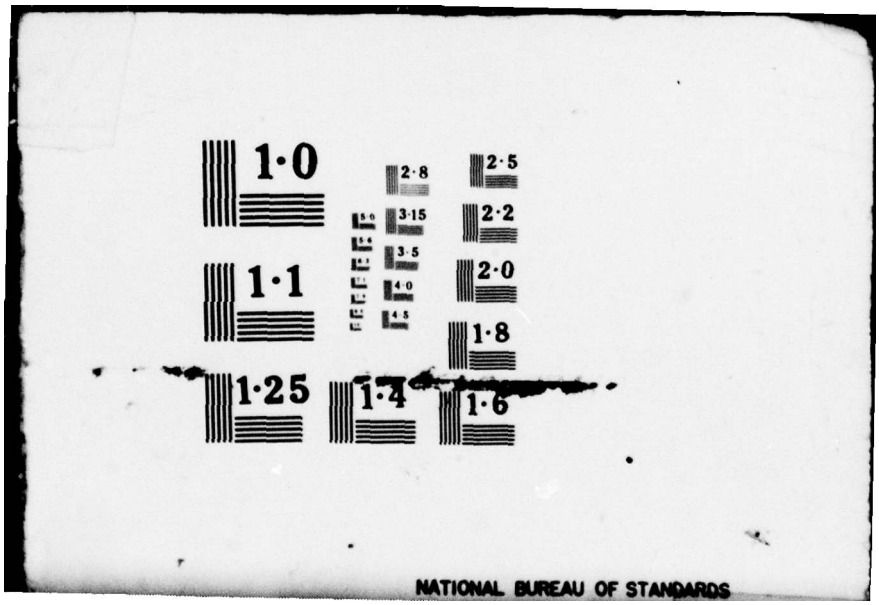
1·0
1·1
1·25
1·4
1·6
1·8
2·0
2·2
2·5
2·8
3·15
3·5
4·0
4·5
NATIONAL BUREAU OF STANDARDS

(12) LEVEL III

DNA 4751F

CAPRI
A Two-Dimensional Eulerian Code for Analyzing the Impact of Highly Deformable Projectiles into Rock

H. E. Read
J. L. Waddell
D. E. Wilkins
R. T. Sedgwick
Systems, Science and Software, Inc.
P.O. Box 1620
La Jolla, California 92038

November 1978

Final Report for Period 15 November 1975—30 September 1976

CONTRACT No. DNA 001-76-C-0151

APPROVED FOR PUBLIC RELEASE;
DISTRIBUTION UNLIMITED.

THIS WORK SPONSORED BY THE DEFENSE NUCLEAR AGENCY
UNDER RDT&E RMSS CODE B344076464 Y99QAXSB04813 H2590D.

Prepared for
Director
DEFENSE NUCLEAR AGENCY
Washington, D. C. 20305

Destroy this report when it is no longer needed. Do not return to sender.

PLEASE NOTIFY THE DEFENSE NUCLEAR AGENCY, ATTN: TISI, WASHINGTON, D.C. 20305, IF YOUR ADDRESS IS INCORRECT, IF YOU WISH TO BE DELETED FROM THE DISTRIBUTION LIST, OR IF THE ADDRESSEE IS NO LONGER EMPLOYED BY YOUR ORGANIZATION.

UNCLASSIFIED

SECURITY CLASSIFICATION OF THIS PAGE (When Data Entered)

REPORT DOCUMENTATION PAGE		READ INSTRUCTIONS BEFORE COMPLETING FORM
1. REPORT NUMBER DNA 4751F	2. GOVT ACCESSION NO.	3. RECIPIENT'S CATALOG NUMBER
4. TITLE (and Subtitle) CAPRI A Two-Dimensional Eulerian Code for Analyzing the Impact of Highly Deformable Projectiles into Rock		5. TYPE OF REPORT & PERIOD COVERED Final Report for Period 15 Nov 75—30 Sep 76 6. PERFORMING ORG. REPORT NUMBER SSS-R-78-3417
7. AUTHOR(s) H. E. Read J. L. Waddell D. E. Wilkins R. T. Sedgwick		8. CONTRACT OR GRANT NUMBER(s) DNA 001-76-C-0151
9. PERFORMING ORGANIZATION NAME AND ADDRESS Systems, Science and Software, Inc. P.O. Box 1620 La Jolla, California 92038		10. PROGRAM ELEMENT, PROJECT, TASK AREA & WORK UNIT NUMBERS NWED Subtask Y99QAXSB048-13
11. CONTROLLING OFFICE NAME AND ADDRESS Director Defense Nuclear Agency Washington, D.C. 20305		12. REPORT DATE November 1978 13. NUMBER OF PAGES 90
14. MONITORING AGENCY NAME & ADDRESS(if different from Controlling Office)		15. SECURITY CLASS (of this report) UNCLASSIFIED 15a. DECLASSIFICATION/DOWNGRADING SCHEDULE

16. DISTRIBUTION STATEMENT (of this Report)

Approved for public release; distribution unlimited.

17. DISTRIBUTION STATEMENT (of the abstract entered in Block 20, if different from Report)

18. SUPPLEMENTARY NOTES

This work sponsored by the Defense Nuclear Agency under RDT&E RMSS Code B344076464 Y99QAXSB04813 H2590D.

19. KEY WORDS (Continue on reverse side if necessary and identify by block number)

Penetration
Finite-Difference Codes
Terradynamics
Soil Mechanics
Sandstone
Eulerian Material Response Codes

20. ABSTRACT (Continue on reverse side if necessary and identify by block number)

A new two-dimensional Eulerian code, CAPRI, is described which was specifically developed to treat the response of highly deformable projectiles impacting rock at normal incidence. Major interest in the study centered around projectiles with soft nose caps, and especially on the influence such nose caps might have in possibly cushioning the response of the projectile aft body.

(over)

DD FORM 1 JAN 73 1473 EDITION OF 1 NOV 65 IS OBSOLETE

UNCLASSIFIED

SECURITY CLASSIFICATION OF THIS PAGE (When Data Entered)

38504

20. ABSTRACT (Continued)

The application of the CAPRI code to numerically analyze the response of a magnesium nose capped cylindrical steel projectile striking sandstone is demonstrated and discussed. Detailed numerical results depicting the configuration of the projectile-sandstone system, and contours of stress in the projectile, at various times after impact are given. Also, time histories of acceleration, velocity, displacement and stress at selected material locations are shown.

The CAPRI code represents an initial attempt to develop an Eulerian numerical code suitable for numerical analysis of such a class of impact problems. It is suggested, however, that further refinements be made in several features of the numerical scheme before the code is made generally available for projectile design studies.

PREFACE

It has been suggested that one possible way of cushioning the impact of an earth penetrating weapon (EPW) striking rock at high velocity may be to add a sacrificial nose cap to the EPW. Such a nose cap would be designed to undergo large plastic flow and fracture during the impact process and, in so doing, dissipate a significant portion of the initial kinetic energy.

The investigation reported herein was part of a larger effort sponsored by the Defense Nuclear Agency, Strategic Structure Division, to examine the feasibility of the sacrificial nose cap concept. The objective of Systems, Science and Software's (S^3) participation in the program was to develop a two-dimensional Eulerian numerical method suitable for analyzing EPW-rock impacts which could be used for parametric studies to perfect the design of sacrificial nose caps. The work performed by S^3 toward this goal is described herein. The Principal Investigator for S^3 was Dr. H. E. Read, and the Project Officer for the DNA was Lt. Col. D. Spangler.

We wish to express our appreciation to Dr. Paul Hadala, U.S. Army Waterways Experiment Station, for his help during the early phases of this work, and for his continuing encouragement throughout. Thanks are also extended to Mr. M. H. Wagner, California Research and Technology (CRT), for helpful conversations pertaining to the CRT sandstone model and for performing a Lagrangian stress propagation calculation using this model to aid us in checking our algorithm for incorporating the model into our Eulerian code.

TABLE OF CONTENTS

LIST OF FIGURES

LIST OF FIGURES (continued)

LIST OF FIGURES (continued)

1. INTRODUCTION

1.1 BACKGROUND

Considerable interest has developed within the defense community during recent years in weapons that are capable of penetrating some distance into the earth before detonating. Such a weapon function is particularly attractive because it (a) reduces the collateral damage produced, and (b) enhances the direct-induced ground shock developed. To be generally effective, earth penetrating weapons (EPW) must be capable of penetrating various geologic targets, ranging from soil to rock, without producing critical damage to the payload. To design weapons with such a mission capability requires knowledge of the intensity of the dynamic loads experienced by the reentry vehicle and its internal components during the penetration process.

The major effort to date to understand projectile penetration reponse has been directed toward soil targets.[1-7] In this case, the hard (usually steel) penetrators undergo relatively small deformation during penetration into soil. An extensive data base on projectile penetration has been accumulated over the years from numerous field tests involving both large and small scale penetrators and a variety of soil targets.

The penetration of projectiles into hard rock is also of defense interest but has received less attention -- both experimentally and numerically -- than soil penetration. In an effort to reduce the intensity of the stress waves that are propagated back into the main body of such a penetrator after impact on rock, several modifications to the basic penetrator design have been proposed. One of these involves attaching a nose cap of different material to the penetrator. The notion behind this concept is that the nose cap material can be designed to undergo large plastic flow and/or fracture

during the penetration process, and in so doing, dissipate sufficient kinetic energy tc cushion the impact process.

In the case of projectiles which are sufficiently hard that they experience very little deformation on impact with rock, the Lagrangian numerical method[8] originally developed for projectile-soil penetration appears to be adequate. However, if on impact with rock a projectile experiences large deformation, the Lagrangian numerical approach described in Reference 8 is inadequate. For such cases, a numerical method is needed that can cope with large plastic deformations accurately, and can also treat the effect of sliding friction, which develops between the penetrator and the rock, on penetrator deceleration.

Unfortunately, none of the existing Lagrangian or Eulerian numerical methods are suitable for this class of impact problems. While Lagrangian methods are capable of treating multiple materials and frictional sliding quite accurately, they are unsuitable for problems involving large plastic flow; although Lagrangian methods are often applied by the defense community to problems involving large plastic deformations, the calculational process usually requires extensive rezoning, and little is known about the credibility (accuracy) of the results so obtained.

The basic strength of the Eulerian method lies in its ability to treat large deformations straightforwardly. On the other hand, the Eulerian method is not particularly well-suited for handling explicit material interfaces, especially those defining free surfaces and sliding interfaces. The Eulerian approach is also susceptible to spurious numerical diffusion, which arises from motion of material through a fixed Eulerian grid. In Lagrangian schemes, on the other hand, the grid is attached to and moves with, the material and consequently there is no mass transport across cell boundaries.

The mass transport procedure typical of most Eulerian schemes requires a mixing between the advected mass and that which remains in a zone; this mixing is responsible for the numerical diffusion, but does tend to stabilize the numerical scheme.

While the Lagrangian and Eulerian methods each have their own characteristic limitations and virtues, we decided to adopt the Eulerian approach in the present effort as the basis on which we would attempt to develop a numerical method suitable for the analyses of penetrator-rock impact. Because of the severe distortion expected to occur in the class of problems of interest to the present study, it was felt that the Eulerian approach would be preferable if the errors due to numerical diffusion did not significantly degrade the numerical solution. Furthermore, an improved mass transport algorithm would be needed to reduce numerical noise generated as material interfaces cross cell boundaries. It was recognized at the outset that, to accomplish this objective would require a number of significant advancements in Eulerian code technology, and the present study was undertaken with this risk in mind.

1.2 SCOPE OF EFFORT

The scope of the effort described herein was limited to (a) the development of a two-dimensional numerical method suitable for analyzing the impact of projectiles with rock targets, and (b) solution of a problem involving the normal impact of a solid projectile having a soft nose cap with hard rock to demonstrate the feasibility and applicability of the new numerical method. Attention was confined to solid projectiles since it was recognized that further advancements in numerical methods, beyond the scope of the present effort, would be required to produce a procedure that would be satisfactory for analyzing the impact reponse of soft nose capped penetrators having thin-walled main bodies.

1.3 SUMMARY OF RESULTS

The main objectives of this study were accomplished, namely (a) a new Eulerian code CAPRI* was developed which is specifically tailored to treat problems involving the normal impact of deformable projectiles with rock, and (b) the application of CAPRI to a projectile-rock impact problem was demonstrated.

The CAPRI code is a two-dimensional Eulerian code developed from the existing HELP code[9] framework. It features the following new capabilities which are evidently important for the class of impact problems of interest to the present investigation:

- Accounts for material strength in mixed-material computational cells.
- Treats frictional sliding between material surfaces in contact.
- Satisfies the correct boundary conditions on stress and velocity at interfaces between materials in contact by equilibrating the normal components of stress and velocity.
- Contains an improved algorithm for transporting mass and other related material properties through the Eulerian grid.
- Accommodates complex geologic material models, including those having a number of history-dependent parameters (see Appendix A for further discussion on this point).

The major portion of study was devoted to the formulation, development and debugging of the intricate numerical algorithms required to incorporate the new features listed above.

To examine and demonstrate the ability of the new code CAPRI to perform numerical analysis of deformable projectile-rock impacts, it was applied to a problem involving a solid

*CAPRI is an acronym for Code for Analysis of Projectile-Rock Impacts.

cylindrical projectile, having a soft magnesium nose cap, impacting sandstone at normal incidence. A numerical solution, which appears to be acceptable, was obtained out to a time after impact (27 μsec) at which a substantial part of the penetration process had occurred. In the process of performing this calculation, however, a number of difficulties with the numerical scheme arose which made it necessary for us to discontinue the calculations. Each time this occurred, the source of the difficulty was uncovered. An appropriate modification was made in the flow field at that time*, and the calculation resumed.

The calculation was not continued beyond 27 μsec because, by this time, the soft magnesium nose cap material had undergone such severe plastic flow that its thickness, in some regions, became less than the Eulerian zone size; this resulted in three materials being present in one zone and, in the present state of development, CAPRI (as well as most Eulerian codes) is unable to adequately cope with such a situation. However, the numerical calculation could have been rather straightforwardly continued by rezoning the Eulerian grid with smaller zones; this was not done.

The work reported here clearly represents only a first step toward developing a numerical method specifically designed for analysis of projectile-rock impacts. To adequately incorporate some of the physical effects felt to be important in such impact problems into the Eulerian framework possibly requires extending the Eulerian method to the limits of its capability. Clearly, there is a need for further investigation of, and improvements in, a number of features of the CAPRI code before it is made available for general use in penetrator design.

*Each time a modification in the flow field was made, it was confined to a single cell. Furthermore, the cells in which such modifications were made were located in regions where their effects probably had negligible influence on the overall deformation and penetration process.

2. NEW FEATURES OF THE CAPRI CODE

The major new capabilities which are available in the CAPRI code are described in this section; these include: (a) an approach for treating frictional sliding, (b) a procedure for incorporating material strength in mixed-material zones, and (c) an improved algorithm for transport of mass and other related material properties.

2.1 FRICTIONAL SLIDING

Eulerian numerical procedures have been developed and incorporated into codes for treating frictionless sliding between materials in contact.[9] In many problems of practical interest which involve the sliding between two metals in contact, the heat generated by the sliding process may produce melting at, and in the vicinity of, the material interface. In many such cases, it can be reasonably assumed that the sliding process is frictionless and this simplification leads, in many instances, to predictions that exhibit reasonable correlation with observations.[9]

For the class of problems of interest to the present study, however, it was felt that the frictional forces due to sliding may have a significant effect on nose cap deformation and overall penetration performance. On this basis, a numerical procedure for treating frictional sliding was developed, incorporated into the CAPRI code, and utilized in the numerical study discussed later in Section 3.

In the sequel, the term "slip cell" is used to denote an Eulerian computational cell which, at the time of interest, contains two materials that may slip relative to each other along their common interface. The sliding materials may be either similar or dissimilar. In the sections which follow, the procedure developed for treating sliding friction in the CAPRI

code is described. Parenthetically, we note that the Eulerian numerical scheme on which CAPRI is based consists of three basic phases, namely, (1) a Lagrangian phase in which the governing equations are treated by disregarding the effect of mass flow, (2) a flow phase in which the material is transported through the fixed Eulerian grid, and (3) a final phase in which the material components in a cell are homogenized. The major revisions to the current Eulerian methodology were made in the Lagrangian and Mass Transport phases, and the details of how this was accomplished are given below.

2.1.1 Equations for Lagrangian Phase

In the CAPRI numerical scheme, the material interface is defined by a string of (passive) tracer particles which are attached to, and move with, the material as it travels through the fixed grid during the deformation process (see Figure 1). To facilitate the treatment of sliding, the interface is considered to be defined by a straight line connecting the points where the tracer string intersects the boundaries of the slip cell, i.e., line ab in Figure 2. The normal and tangential directions are defined in terms of the angle θ which the line ab makes with the radial axis.

Figure 3 depicts the stresses acting on each of the two material elements occupying a typical slip cell. Across the common material interface the tangential component of velocity V_t, is in general, discontinuous, while the following continuity conditions hold for the normal stress σ_n, the tangential shear stress, τ, and the normal component of velocity V_n;

$$\left.\begin{aligned} (\sigma_n)_1 &= (\sigma_n)_2 \\ \tau_1 &= -\tau_2 \\ (V_n)_1 &= (V_n)_2 \end{aligned}\right\} \qquad (1)$$

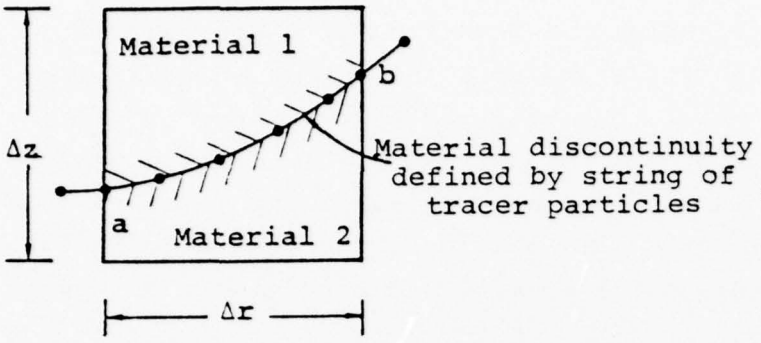

Figure 1. Mixed Eulerian cell with slip interface.

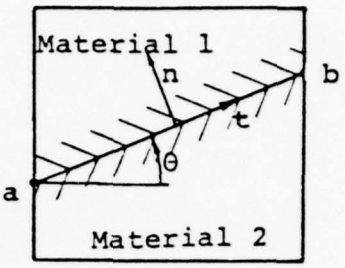

Figure 2. Idealization of slip interface employed in sliding algorithm.

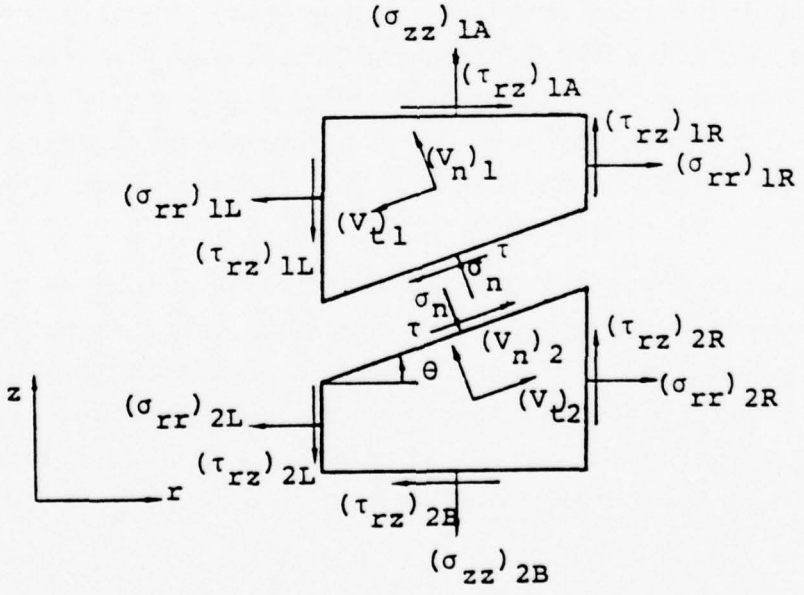

Figure 3. Stress components acting upon material elements in a slip cell.

Here, and in that which follows, the subscript 1 refers to material 1 and subscript 2 to material 2. Upon applying the law of motion over a time interval Δt to each of the material elements, the following system of linear equations result which govern the motion of the material elements during the Lagrangian phase of the numerical scheme:

$$\tilde{U}_1^{n+1} + \left(\frac{\Delta t}{m_1} \sin \theta A_i\right)\sigma_n - \left(\frac{\Delta t}{m_1} \cos \theta A_i\right)\tau = \left(U_1^n + \frac{\Delta t}{m_1} F_1^n\right) \tag{2}$$

$$\tilde{V}_1^{n+1} - \left(\frac{\Delta t}{m_1} \cos \theta A_i\right)\sigma_n - \left(\frac{\Delta t}{m_1} \sin \theta A_i\right)\tau = \left(V_1^n + \frac{\Delta t}{m_1} F_2^n\right) \tag{3}$$

$$\tilde{U}_2^{n+1} - \left(\frac{\Delta t}{m_2} \sin \theta A_i\right)\sigma_n + \left(\frac{\Delta t}{m_2} \cos \theta A_i\right)\tau = \left(U_2^n + \frac{\Delta t}{m_2} F_3^n\right) \tag{4}$$

$$\tilde{V}_2^{n+1} + \left(\frac{\Delta t}{m_2} \cos \theta A_i\right)\sigma_n + \left(\frac{\Delta t}{m_2} \sin \theta A_i\right)\tau = \left(V_2^n + \frac{\Delta t}{m_2} F_4^n\right) \tag{5}$$

Here, m_1 and m_2 denote the masses of the material elements occupying the slip cell at time t^n, and A_i is the surface area of the interface between the materials at t^n. The tilde is placed above the velocity symbols to denote their values at the end of the Lagrangian phase. Finally, the forces F_i^n are defined by the following equations:

$$\left.\begin{aligned}
F_1^n &= (\sigma_{rr})_{1R} A_{1R} - (\sigma_{rr})_{1L} A_{1L} + (\tau_{rz})_{1A} A_{1A} \\
&\quad - (\tau_{rz})_{1B} A_{1B} - (\sigma_{\theta\theta})_1 A_1 \\
F_2^n &= (\sigma_{zz})_{1A} A_{1A} - (\sigma_{zz})_{1B} A_{1B} + (\tau_{rz})_{1R} A_{1R} - (\tau_{rz})_{1L} A_{1L} \\
F_3^n &= (\sigma_{rr})_{2R} A_{2R} - (\sigma_{rr})_{2L} A_{2L} + (\tau_{rz})_{2A} A_{2A} \\
&\quad - (\tau_{rz})_{2B} A_{2B} - (\sigma_{\theta\theta})_2 A_2
\end{aligned}\right\} \tag{6}$$

$$F_4^n = (\sigma_{zz})_{2A} A_{2A} - (\sigma_{zz})_{2B} A_{2B} + (\tau_{rz})_{2R} A_{2R} - (\tau_{rz})_{2L} A_{2L}$$

where all quantities to the right of the equal signs are evaluated at time t^n, and the A's denote partial areas.

Upon requiring equality between the normal components of velocity for both materials, one obtains the expression:

$$\tilde{U}_1^{n+1} \sin\theta - \tilde{V}_1^{n+1} \cos\theta = \tilde{U}_2^{n+1} \sin\theta + \tilde{V}_2^{n+1} \cos\theta = 0 \qquad (7)$$

To complete the above system of equations, the dependence of the frictional shear stress τ on the other independent variables must be prescribed. In a related DNA-sponsored program, a series of experiments was performed by S^3 to characterize the frictional shear stress developed between steel and rock during high speed sliding.[10] Experimental results were obtained in this study for sliding velocities up to 3000 cm/sec and for normal stresses up to about 1 kbar. Within this range of sliding velocities and normal stresses, the frictional shear stress, τ, in all cases studied was found to obey the law:

$$\tau = \mu \sigma_n \exp\left(-\frac{C\sigma_n}{\xi}\right) \qquad (8)$$

where C denotes the sliding velocity, σ_n is the stress normal to the direction of sliding, and μ and ξ are material-dependent parameters. For the class of defense-related impact problems of interest to the present study, the sliding velocities and normal stresses lie well beyond the range covered by the experiments noted above. In such cases, it can be argued[10] that the frictional resistance will most likely be less than that indicated by the low velocity-low stress laboratory tests, and also exhibit only a weak dependence on sliding velocity. On this basis, the following expression was proposed in Reference 11 and adopted in the present study to describe the frictional shear stress τ developed between steel and Dakota sandstone for high velocity-high stress conditions:

$$\tau = a \sigma_n \exp(-\sigma_n/b) \quad \text{for } \sigma_n > 0 \qquad (9)$$

Here, a = 0.19 and b = 1.6 kbars. Equation (9) prevents an unlimited buildup of frictional stress, reaching a peak value of 0.112 kbars at σ_n = 1.6 kbars. In the CAPRI numerical scheme, Equation (9) is described by the following expression:

$$\tau = \text{sign}\ \{(V_t^n)_2 - (V_t^n)_1\}\ F(\sigma_n) \tag{10}$$

which provides the proper sign of τ in terms of the tangential velocities. The function $F(\sigma_n)$ is defined by:

$$F(\sigma_n) = a\sigma_n \exp\ (-\sigma_n/b) \tag{11}$$

where the values of the constants a and b are listed above.

Equations (2) to (5), (7) and (10) form a system of six linear equations which is solved in the CAPRI code by matrix inversion to yield the values of the six unknowns $\tilde{U}_1^{n+1}$, $\tilde{V}_1^{n+1}$, $\tilde{U}_2^{n+1}$, $\tilde{V}_2^{n+1}$, σ_n and τ at the end of the Lagrangian phase of the calculation.

2.1.2 Calculation of the Deviatoric Strain Rates for Materials in Slip Cells

As noted above, the preceding equations apply to the Lagrangian phase of the Eulerian numerical scheme, and they ensure that the basic conditions which apply at material interfaces [see Eq. (1)] are satisfied during this phase of the calculation. In order to equilibrate the normal stress components after the mass transport phase, one must calculate the strain rates for each material in the slip cell. This is not a trivial task, since the material interface is a surface across which the strain tensor, and consequently the deviatoric strain rates, are discontinuous.

A procedure was developed for the CAPRI code which provides an approximate method for calculating the deviatoric strain rates in each slip cell material; this approach utilizes

the velocity components of a material element in the slip cell, as well as those of the same material in neighboring cells, to calculate the deviatoric strain rates for that material. The procedure is clearly most accurate when the material interface passes through, or near, the cell center, and becomes more approximate as the position of the interface deviates further from this condition.

2.1.3 Equilibration of Normal Stress Components After Mass Transport Phase

After completion of the mass transport phase, the code utilizes an iteration procedure to equilibrate the normal components of stress in the two slip-cell materials. In the iteration scheme, the deviatoric strain rates, determined by the method described in Section 2.1.2, remain fixed and the densities of the two materials in the mixed cell are adjusted until the components of stress normal to the interface are equal. The present iteration scheme is particularly tailored to treat the case of interest herein in which one of the sliding materials is a metal and the other a rock material. A rock-type constitutive model introduces considerable complexities into the iteration procedure because, for such materials, the hydrostatic and deviatoric components of stress are usually coupled through the dependence of the yield strength on pressure.

After the procedure for treating frictional sliding between materials, described in the preceding sections, had been incorporated into the CAPRI code, a simple two-material problem, for which a theoretical solution could be obtained to check the numerical results, was analyzed with the new code. A description of this analysis, and the corresponding results obtained are provided in Appendix B. As shown there, the agreement between the theoretical and numerical solutions is excellent.

2.2 MASS TRANSPORT

2.2.1 Shortcomings of Existing Methods

In state-of-the-art Eulerian codes such as HELP,[9] the mass flux, Δm_i, of material i through a boundary of a mixed material cell is usually given by an expression of the form:

$$\Delta m_i = \rho_i \bar{v}_i \, A_i \Delta t \tag{12}$$

where ρ_i denotes the donor cell density, $\bar{v}_i$ is an interpolated velocity representing the velocity normal to that boundary at the end of the time step Δt, and A_i represents that portion of the area of the cell boundary intersected by material i. The area A_i is determined by tracer particle positions.

There are several shortcomings in the mass transport algorithm described above. In the first place, substantial inaccuracies can arise in the calculation of mass fluxes as a material interface crosses over an entire cell boundary during a single time step. To illustrate this, consider Figure 4 which shows the positions of a material interface before and after it crossed a cell boundary at times t and $t+\Delta t$, respectively. According to the interface position at time t, the cell boundary is intersected only by material 2. Thus, on the basis of the algorithm discussed above, the area for material 1, A_1, is zero and no material 1 is transported across the boundary. It is obvious, however, from the position of the interface at time $t+\Delta t$ that some material 1 has entered the cell. Moreover, it is necessary to reduce the flux of material 2 as calculated by Eq. (12) since, for this case, there is generally less mass of material 2 in the cell than is calculated.

Another difficulty may occur if an interface leaves a cell and the flux of material calculated by Eq. (12) is insufficient to evacuate all of that material from that cell, i.e., some of the material is left behind. In this case, special

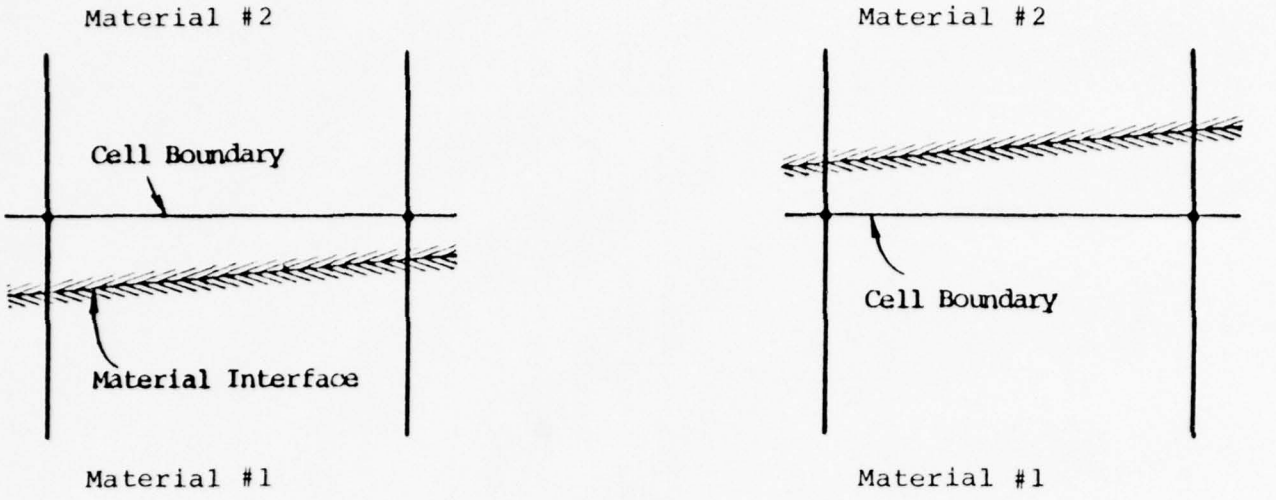

(a) Position at time t^n

(b) Position at time $t^n+\Delta t$

Figure 4. Material interface crossing a cell boundary.

procedures are usually employed to increase the flux so that all of the material is evacuated.

Since the difficulties noted above vanish as the time step becomes very small, subcycling procedures have been introduced to reduce errors in transport across mixed-material cell boundaries. This is accomplished by using N time steps for mass transport calculation within each normal time step Δt. The number N is selected by the user, and, in practical applications, is usually taken to fall in the range $2 \leq N \leq 4$. One disadvantage of subcycling, of course, is that it can increase significantly the cost of a calculation. Furthermore, although the errors in transport are substantially reduced, they are not eliminated; they are usually small and are quickly damped by the spurious numerical diffusion characteristic of Eulerian codes.

2.2.2 New Algorithm for Mass Transport

In the course of the present program, it was found that the mass transport algorithm described above was unsatisfactory for the class of impact problems of interest. In particular, the relatively low stresses generated by projectile-rock impacts were significantly perturbed by the relatively large numerical errors generated as material interfaces crossed cell boundaries. Futhermore, the history-dependent parameters in the sandstone model made it "remember" the non-physical states it passed through, thus further degrading the reliability of the results obtained. Since the number of "subcycles" of the multimaterial cell mass transport algorithm necessary to reduce these errors to an acceptable level would have made the calculation prohibitively expensive to do, it was decided to attempt to improve the algorithm.

The improvement essentially involves a redefinition of the area term, A_n, in Equation (12) whenever either of the two

problem cases discussed previously are encountered. In each case, Δm_n, the mass flux, is considered to be known, i.e., it is the total amount of mass of material n remaining in the cell. Then the area term is defined to be the value necessary to satisfy Equation (12):

$$A_n = \Delta m_n / \rho_n \, \bar{v}_n \, \Delta t. \tag{13}$$

The area terms for any other materials which intersect that cell boundary are now proportionally adjusted to satisfy the constraint:

$$\sum_n A_n = A \tag{14}$$

where A is the total area of the cell face.

The algorithm described above was incorporated into the CAPRI code and used along with "subcycling" on several test problems involving vertical, horizontal and diagonal movement of a solid bar in uniform motion surrounded by a free surface. Virtually no numerical noise was generated by the improved mass transport algorithm.

2.3 MATERIAL FAILURE

The problems considered in the present study are characterized by extensive failure of material. The penetration of a projectile into rock is accomplished through extensive fracturing and comminution of the rock. Furthermore, the severe deformations that soft nose caps will likely experience during penetration can be expected to far exceed the failure threshold of the material.

Regions of failed material move through an Eulerian grid as a result of (a) further cracking and failure, and (b) advection of material. An approximate method was developed and incorporated into the CAPRI code to (a) reduce the

effect of numerical diffusion on the identification of regions of failure and (b) allow for the effect of failure on material properties. This was accomplished through the introduction of a flow field fracture variable F. This variable is a material property which characterizes the failure state of a material. If the material in a zone is unfractured, F = 1, while F = 0 for a zone occupied by fractured material only. For zones containing both fractured and unfractured material, the value of F lies somewhere between zero and unity. Since F is a material property, it is transported through the Eulerian grid in the same manner as the stress deviators.

As presently structured, the CAPRI code assumes that failed material is unable to support deviatoric stresses. Accordingly, in zones containing both failed and unfailed material, i.e., where $0 \leq F \leq 1$, the shear modulus G and yield strength Y are reduced proportionately in the following manner to reflect the degradation in material strength:

$$G = FG_0$$
$$Y = FY_0 \qquad (15)$$

Here, F denotes the fraction of failed material in the zone, and G_0 and Y_0 represent, respectively, the initial unfailed values of the shear modulus and yield strength.

3. NUMERICAL STUDY OF NOSE-CAPPED PROJECTILE IMPACTING ROCK

A two-dimensional numerical study was performed with the new CAPRI code to examine, and to demonstrate, its ability to analyze the response of highly deformable projectiles striking rock. The details of the study are given in this section.

3.1 DESCRIPTION OF IMPACT PROBLEM

Figure 5 depicts the initial axisymmetric configuration of the projectile-rock impact problem considered in the numerical study. The projectile consisted of a solid cylinder of D6A-C steel to which a soft magnesium alloy nose cap of the same diameter was attached. The diameter of the projectile was 2 cm and its overall length was 4 cm. The nose cap was 1 cm thick. It was assumed in the numerical study that the nose cap and the main body remained permanently bonded together during the penetration process; frictional sliding took place only between the sandstone and projectile. The impact velocity was 6×10^4 cm/sec. The numbered locations in Figure 5 denote the initial positions of Lagrangian points which identify the material positions at which time histories of the flow field variables were monitored throughout the calculation.

The Eulerian grid used to obtain the numerical results reported herein is shown in Figure 6. In all, a total of 3,000 computational zones was employed.

3.2 CONSTITUTIVE MODELS

3.2.1 Projectile and Nose Cap

The constitutive behavior of the projectile and nose cap materials was described by simple elastic-ideally plastic models. Material property data for D6A-C steel was obtained from Reference 12 and corresponding data for the magnesium alloy AZ80A-T5 was found in Reference 13. Because of the relatively low stress levels expected in the class of problems of interest, a simple equation of state of the form:

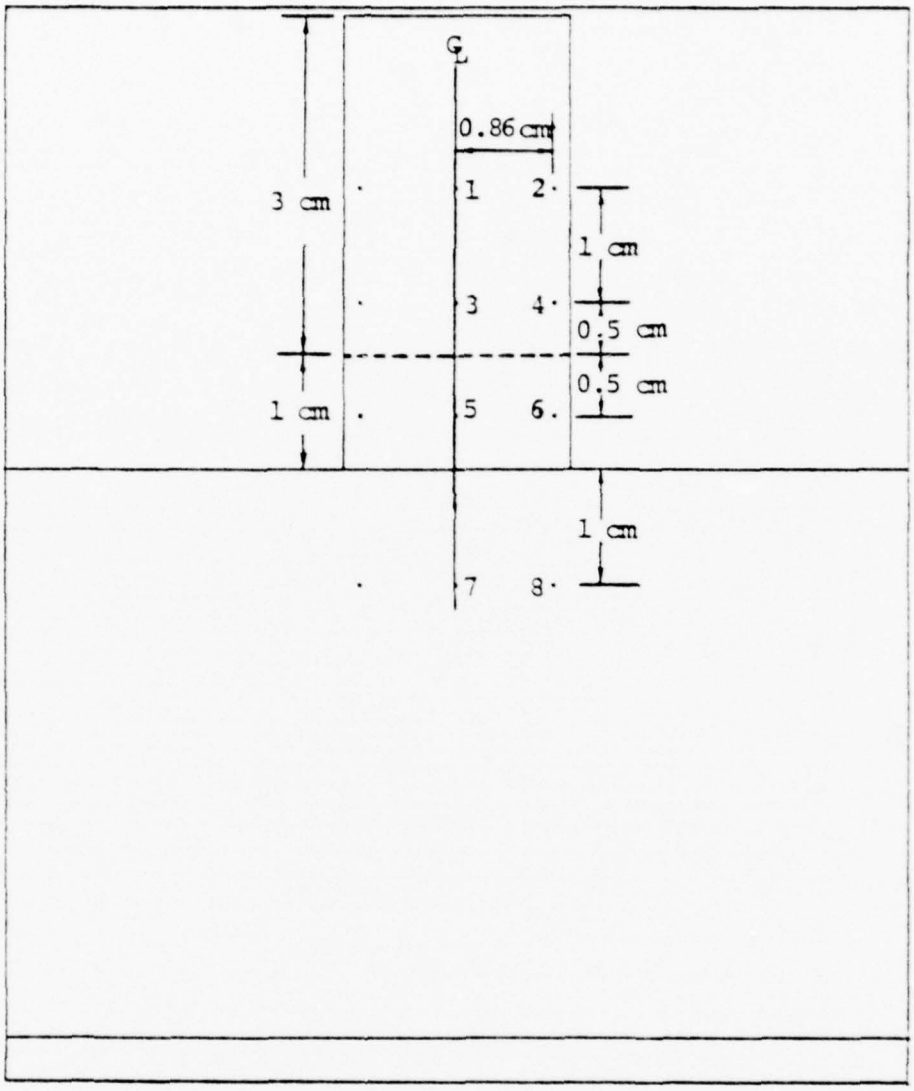

Figure 5. Initial projectile-target configuration showing the gauge positions where stress histories were monitored. The dashed line indicates the initial position of the interface between the projectile body and the magnesium nose cap.

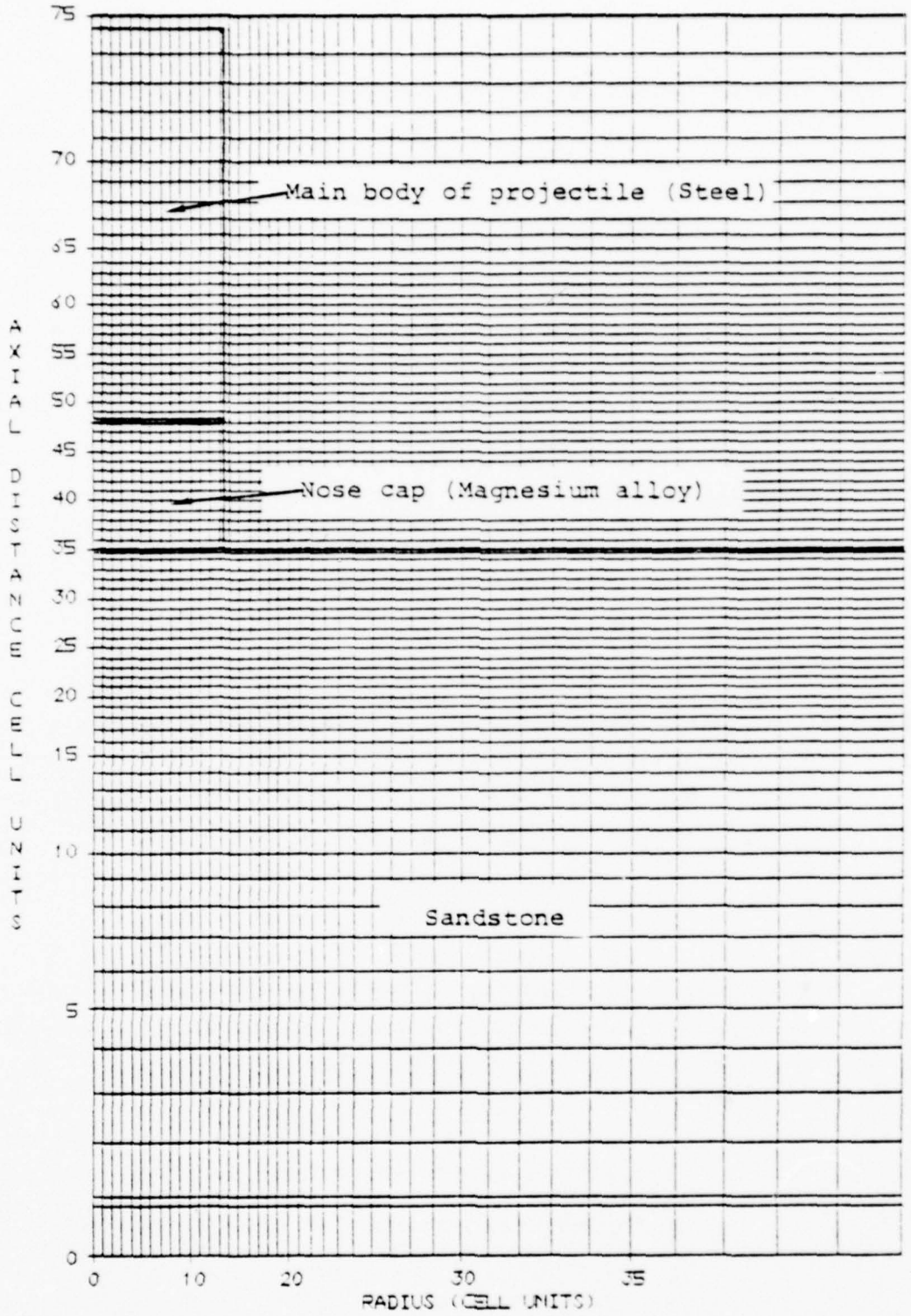

Figure 6. Computational grid selected for numerical study.

$$P = K(\rho/\rho_o - 1) \qquad (16)$$

was employed. Here, K denotes the bulk modulus, ρ is the density, and ρ_o is the initial value of the density. If the accumulated generalized plastic strain in a material element reached a prescribed level, the material was assumed to fracture; when this occurred, all components of the deviatoric stress tensor were reduced to zero (see Section 2.3).

The values of the material parameters used for projectile materials in the numerical study are summarized in Table 1.

3.2.2 Rock

Dakota sandstone was selected for the numerical study because it typifies the kinds of rock materials found at many hard sites of defense interest. Furthermore, the complex behavior of Dakota sandstone has been rather extensively investigated in the laboratory by the U.S. Army Waterways Experiment Station and Terra Tek,[14] and recently a constitutive model for this material was developed by CRT.[11] The CRT model describes the complex plastic behavior of Dakota sandstone within an elastic-plastic framework; it requires knowledge of a number of history-dependent parameters, including the pressure, the extent of fracture and the generalized plastic strain. Provision is made in the model for describing post-fracture response, wherein the strength of the fractured material is degraded to that characteristic of the fully crushed condition. In most regions of behavior, the model uses an associated flow rule; however, under certain conditions, a non-associated rule is employed; this model has been employed in several Lagrangian numerical studies performed by CRT, and appears to provide a reasonably satisfactory description of the constitutive behavior of this material.

The CRT model requires information on the current values of six history-dependent material parameters which, of course,

Table 1

Material Properties of Projectile Materials

Material Property	Magnesium Alloy AZ80A-T5	D6A-C Steel
Mass density ρ (gm/cm^3)	1.8	7.85
Bulk modulus K ($dynes/cm^2$)	3.89×10^{11}	1.668×10^{12}
Shear modulus G ($dynes/cm^2$)	1.71×10^{11}	7.888×10^{11}
Yield stress Y_o ($dynes/cm^2$)*	2.60×10^{9}	13.0×10^{10}
Generalized plastic strain fracture threshold, $\bar{\varepsilon}^p$	0.0142	0.0940

* Y_o denotes the yield stress in simple tension.

are associated with given (identifiable) material elements. In a Lagrangian formulation, material elements maintain their identity throughout a calculation, and the task of keeping track of history-dependent material parameters associated with such elements poses no special problems. In an Eulerian formulation, however, the task is more complex since the basic formulation is not designed to maintain the identity of individual material elements. Because of this, there was some uncertainty at the outset of the study as to the accuracy that could be achieved in treating such a complex, history-dependent material model with an Eulerian framework, and a part of the effort was devoted to addressing this question.

In the course of the present study, we found that the complex CRT sandstone model could be adequately treated in the Eulerian CAPRI code framework if the six history-dependent material parameters were incrementally updated in the numerical scheme by the same approach used to update the deviatoric stresses (see Ref. 9 for details of procedure for updating deviatoric stress components). To demonstrate the accuracy of this procedure, a one-dimensional wave propagation problem was formulated as a test case,[15] and analyzed independently by CRT,[16] using their WAVE-L Lagrangian code, and by S^3, with the Eulerian CAPRI code. The specific details of the impact configuration considered by both CRT and S^3 are given in Appendix A, together with the numerical results from both calculations. An inspection of these results shows that the calculated stress wave profiles from both computations are in reasonable agreement, and, thus, demonstrates the accuracy with which the Eulerian CAPRI code can treat a complex, history-dependent constitutive model.

3.3 EARLY TIME ONE-DIMENSIONAL SHOCK STATES

Under the assumption of uniaxial stress, the shocked states produced in the sandstone, magnesium and steel by the impact can be determined analytically, and used to check,

where appropriate, the calculational results. A plot of the Hugoniots for sandstone, magnesium and steel appropriate for the material configuration and impact velocity of interest is given in Figure 7. As this figure reveals, the sandstone Hugoniot intersects the reflected steel Hugoniot at a stress of approximately 26 kbars. In addition, the figure shows that the shock transmitted from the sandstone-magnesium interface produces a shock in the steel of approximately 29 kbars. Thus, on the basis of one-dimensional shock propagation theory, which is valid only at early times near the axis at the sandstone-magnesium interface, it is concluded that the use of a soft nose cap causes the shock transmitted back into the steel main body to be greater than if there were no nose cap. Conversely, if the nose cap had been fabricated from a material which is harder than steel, such as a tungsten alloy for example, similar one-dimensional considerations indicate that the stress propagated into the steel body would be less than if (a) the nose cap was made from a material softer than steel, and (b) there was no nose cap. This result follows from Figure 8, where the appropriate Hugoniots for sandstone, steel and a tungsten alloy are shown.

It should be emphasized that the above conclusions apply only to sandstone targets, and to other rock materials that exhibit Hugoniots which are less stiff than sandstone. For rocks having sufficiently stiffer Hugoniots than sandstone, it can be shown, using similar arguments, that a soft nose cap serves to reduce the transmitted stress levels.

Whether or not the above conclusions also hold when two-dimensional effects are taken into consideration is not known; their validity could be investigated by performing a similar numerical calculation with the CAPRI code for a steel projectile without a nose cap, and comparing the stress levels generated in the steel with those determined for the magnesium capped projectile in the present study.

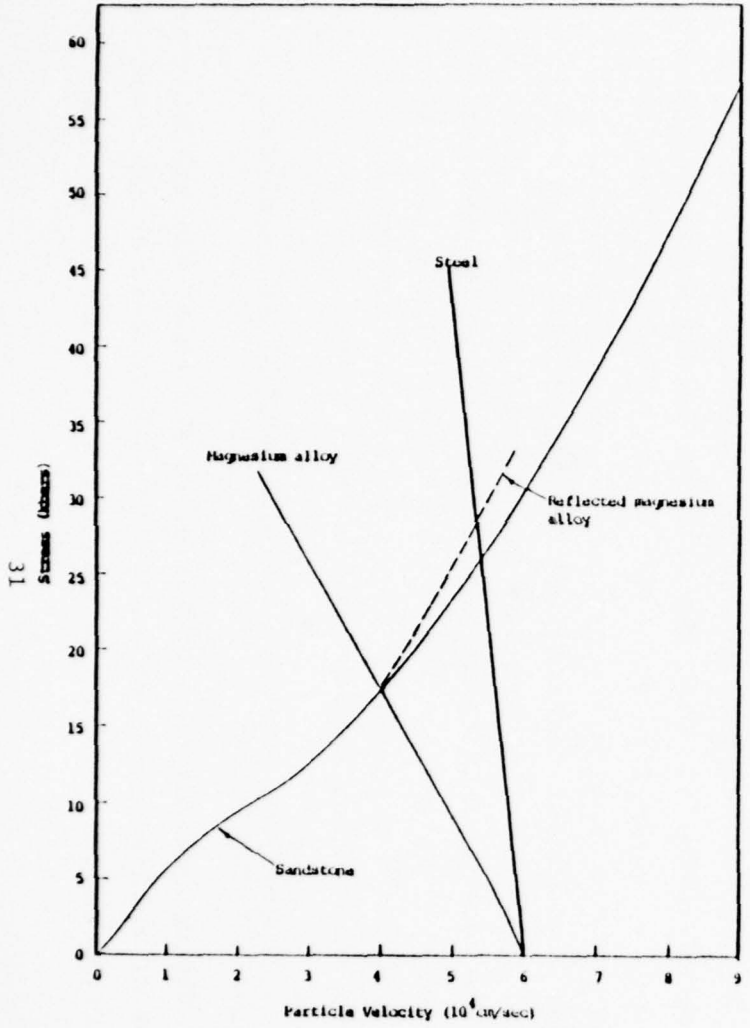

Figure 7. Stress vs. particle velocity relationships of sandstone, magnesium alloy and steel for initial impact velocity of 6 x 10^4 cm/sec.

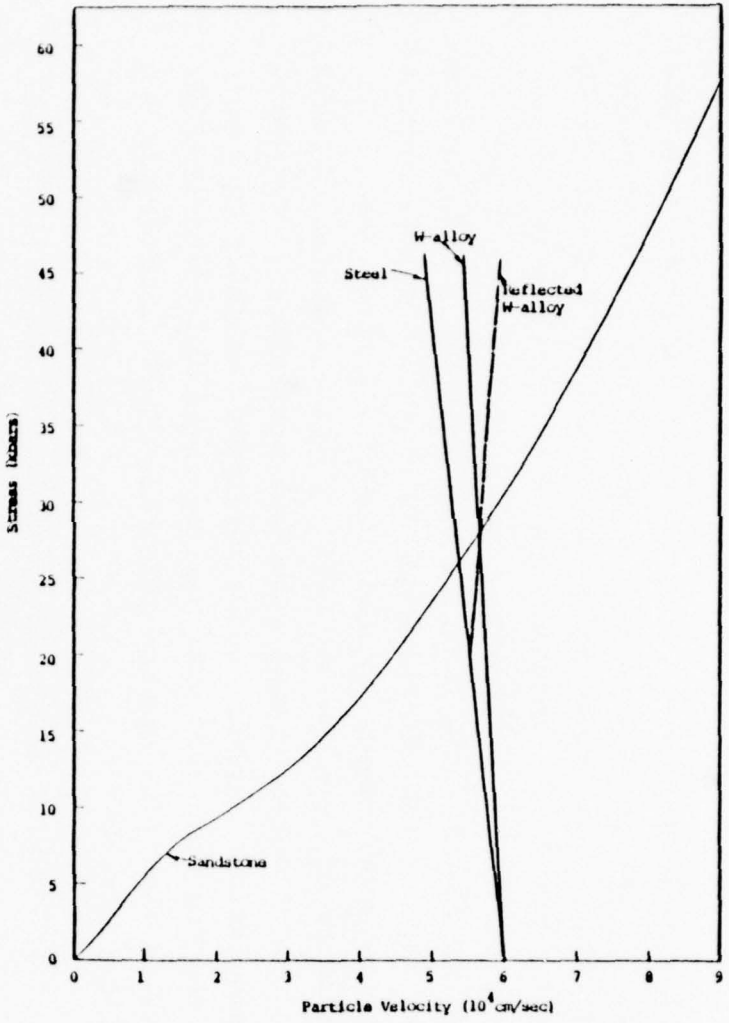

Figure 8. Stress vs. particle velocity relationships of sandstone, a tungsten alloy and steel for initial impact velocity of 6 x 10^4 cm/sec.

4. NUMERICAL RESULTS

The results obtained from the numerical study described in Section 3 are presented here. As noted earlier, the numerical calculation was taken out to 27 μsec after impact. At this time, significant deceleration of the projectile had not taken place, but the soft magnesium nose cap had undergone such severe plastic flow that its thickness had become smaller than the size of the calculational Eulerian zone; this resulted in three materials being present in a single zone, and in the current state of development, CAPRI, as well as Eulerian codes, is unable to adequately cope with such a situation. The numerical calculation, however, could have been continued by rezoning the Eulerian grid with smaller zones and continuing the calculation, but this was not attempted due to limitations of remaining funds.

4.1 CONFIGURATION OF SYSTEM AT VARIOUS TIMES AFTER IMPACT

Figures 9 and 10 depict the calculated configurations of the projectile-rock system at various times after impact up to the time (27 μsec) at which the calculation was discontinued. Also shown in these figures is the progressive development of failure regions in both the projectile and rock materials. Although significant deceleration of the projectile had not occurred by 27 μsec, severe distortion and flow of the soft magnesium nose cap has taken place. By 3 μsec, the nose cap had completely failed and its thickness was reduced to a thin layer of flowing metal by 27 μsec. Note also that some failure has also taken place in the steel at this time.

4.2 ACCELERATION, VELOCITY AND DISPLACEMENT AT SELECTED LAGRANGIAN POINTS

The calculated time histories of the axial and radial components of acceleration, velocity and displacement at the most interesting Lagrangian gage points noted in Figure 5 are depicted

in Figures 11 to 22. The response at Gage 5 is of particular interest, since the early-time deformation at this location is uniaxial strain until relief waves arrive from the free surface. Comparison of the calculated peak velocity at early times, shown in Figure 16, with the analytically determined velocity given in Section 3.3 shows good agreement. The reason for the gradual increase in the axial velocity at Gage 5 at later times (say past 10 μsec) is not known, however; this could be the result of complex wave interactions within the magnesium, or be due to features of the numerical scheme. The accuracy with which the code can treat the response of the magnesium nose cap undoubtedly decreases as the magnesium is further deformed into a thin layer. Inspection of the velocity and displacement histories in the magnesium at Gage 5, shown in Figures 16 and 17, indicates no significant deceleration of the projectile has occurred by 27 μsec. However, the velocity history for Gage 3, shown in Figure 12, reveals that there has been some small deceleration of the steel main body.

4.3 STRESS HISTORIES AT SELECTED LAGRANGIAN POINTS

The calculated time histories of the axial stress σ_z, the radial stress σ_r, the hoop stress σ_θ and the shear stress τ_{rz} at the most interesting Lagrangian points are presented in Figures 23 to 28. For the Lagrangian points which lie on the axis, the conditions $\sigma_r=\sigma_\theta$ and $\tau_{rz}=0$ hold. Here, and in that which follows, compressive stresses are taken as positive.

Consider now the calculated stress histories in the steel main body at Gage 3, which are shown in Figure 23. The early-time axial stress response shows a peak of about 8 kbars which is considerably smaller than the 29 kbar stress level predicted in Section 3.3 on the assumption of one-dimensional deformation. It is thus concluded that the early time response is not one-dimensional, but is influenced strongly by the arrival of relief

waves. At later times, the axial stress increases up to about 14 kbars possibly as a result of complex interaction between waves contained within the steel main body.

The stress histories in the magnesium at Gage 5 are shown in Figure 25. At early times, the response at this location is one-dimensional. The calculated peak axial stress when one-dimensional conditions prevail is 15.8 kbars which compares well with the value of 17 kbars determined from Figure 7 in Section 3.3. The magnesium in the neighborhood of the gage fails at about 1.5 μsec, and thereafter behaves as a strengthless solid. After the initial pulse, the axial stress increases up to a nominal level of about 18 kbars at late times. The cause of this rise in axial stress is not currently known. As noted earlier in Section 4.2, it may result from wave interactions within the magnesium, or be due to possible deficiencies in the numerical scheme for dealing with the nose cap material as it deforms into a layer which has a thickness on the order of the zone size.

In Figure 27, the stress histories in the sandstone at Gage 7 are shown. Again, the calculated peak axial stress of about 8 kbars at early times is substantially smaller than that predicted by one-dimensional considerations in Section 3.3. Thus, the early time response at this location also appears to be significantly affected by relief waves.

Finally, the stress histories at the off-axis Lagrangian locations are given in Figures 24, 26 and 28.

4.4 STRESS CONTOURS IN THE PROJECTILE AT SEVERAL TIMES AFTER IMPACT

In order to depict the evolution of stress distribution in the projectile contours showing the stress fields in the projectile at 5, 15 and 25 μsec after impact are presented in Figures 29 to 31. In each figure, contours of the radial stress σ_r, the hoop stress σ_θ, the axial stress σ_z, and the shear stress

τ_{rz} are shown separately. The contour intervals are two kbars, except in the case of the shear stress where they are one kbar.

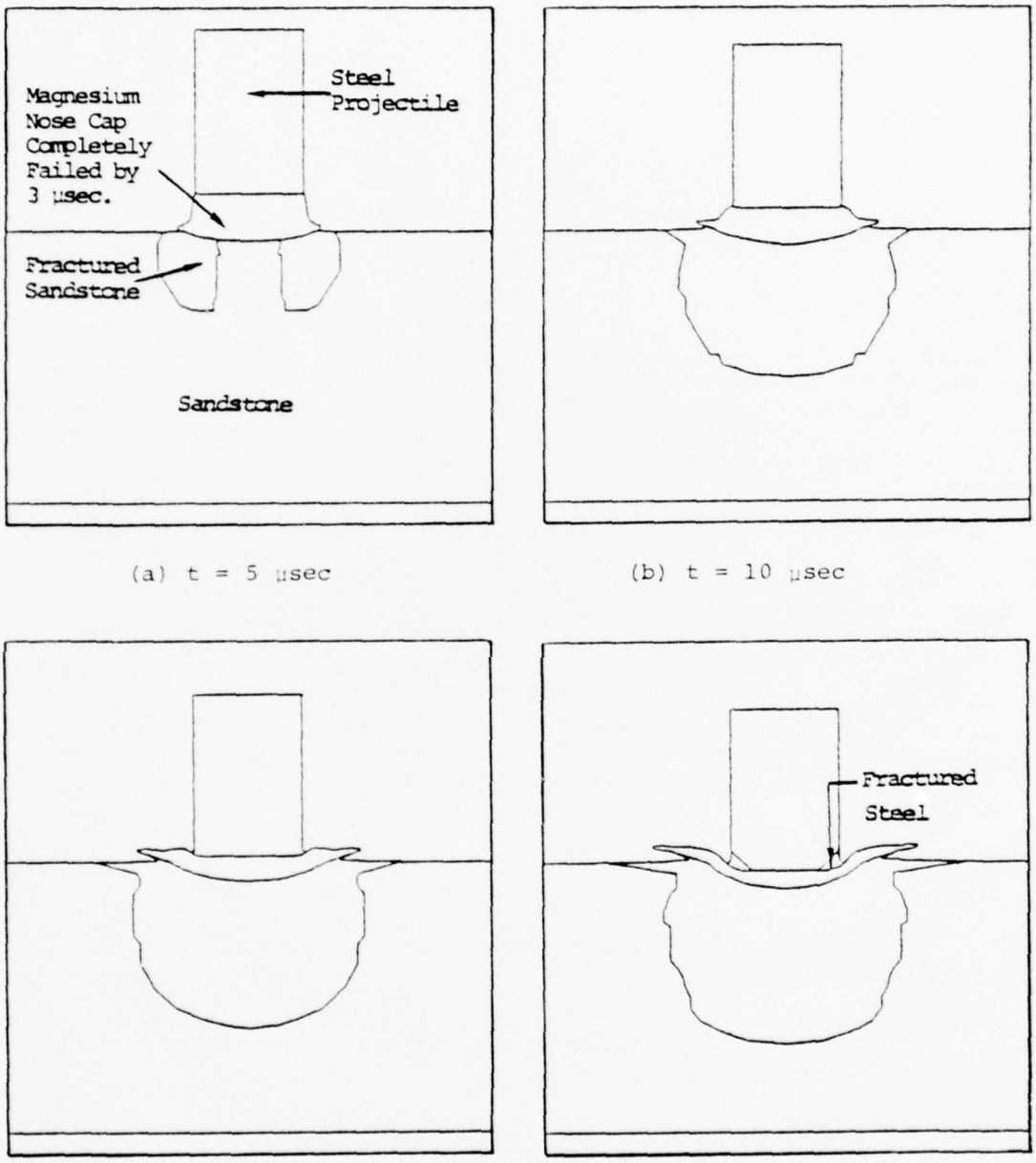

(a) t = 5 μsec

(b) t = 10 μsec

(c) t = 15 μsec

(d) t = 20 μsec

Figure 9. Projectile-rock configuration at various times after impact, showing region of failed material.

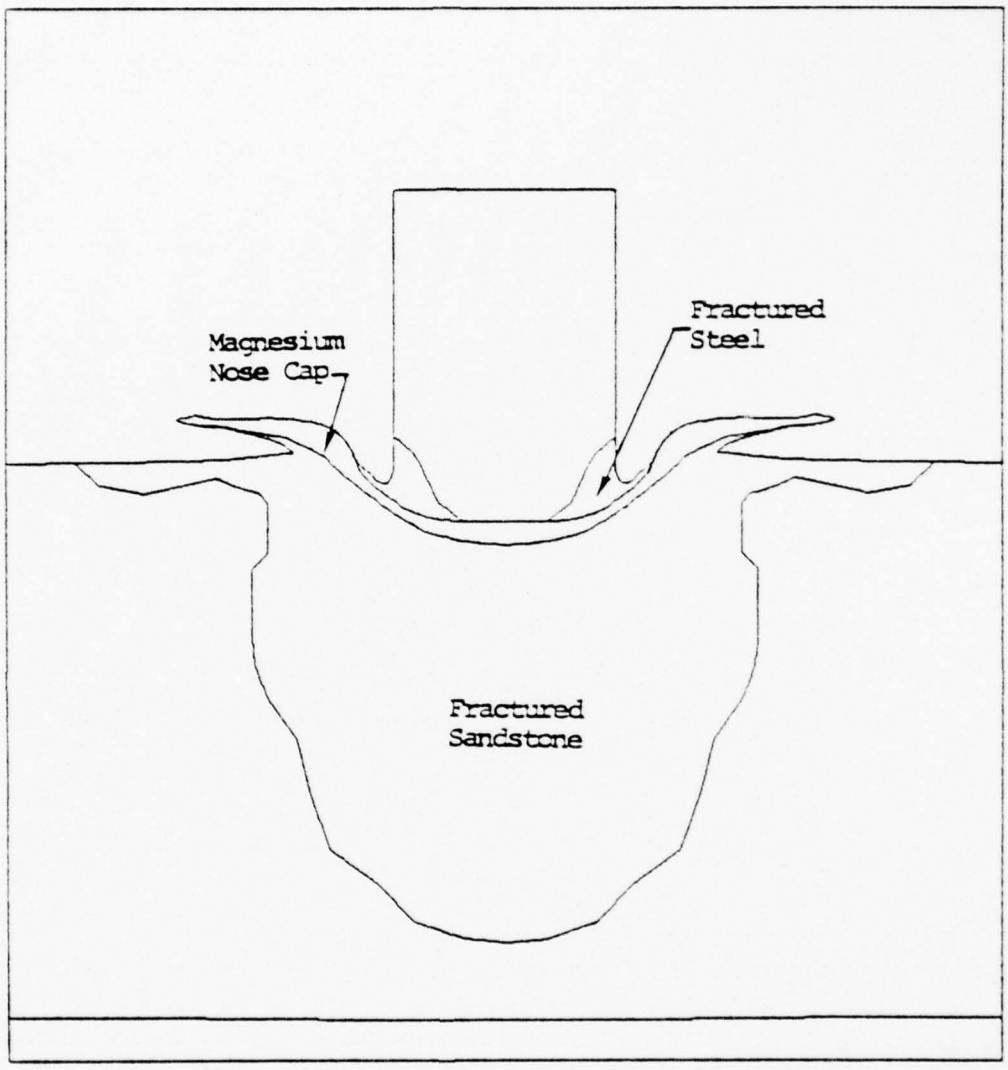

Figure 10. Projectile-rock configuration at the time the calculation was discontinued, i.e., 27 μsec.

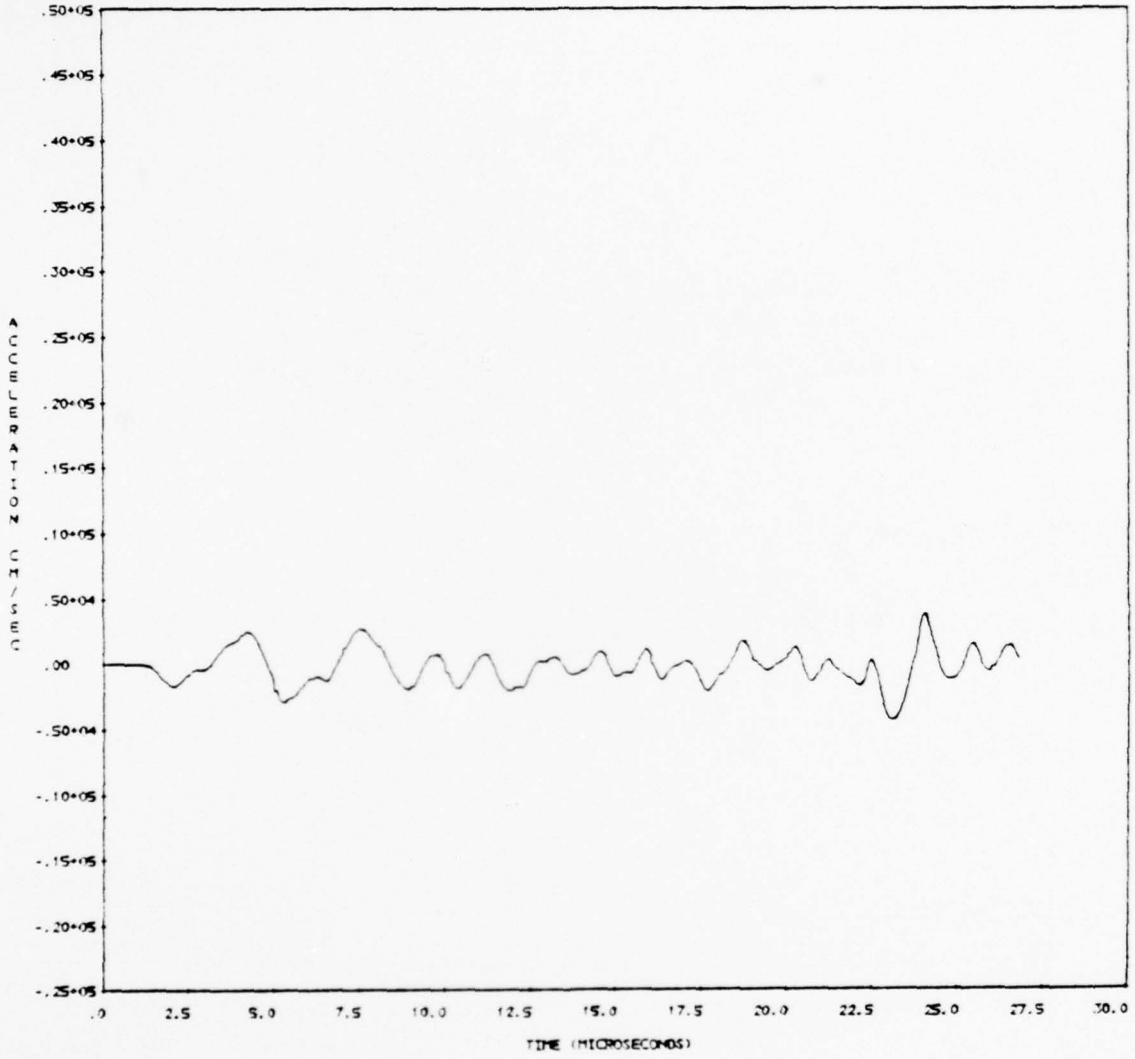

Figure 11. Axial acceleration history at Gage 3.

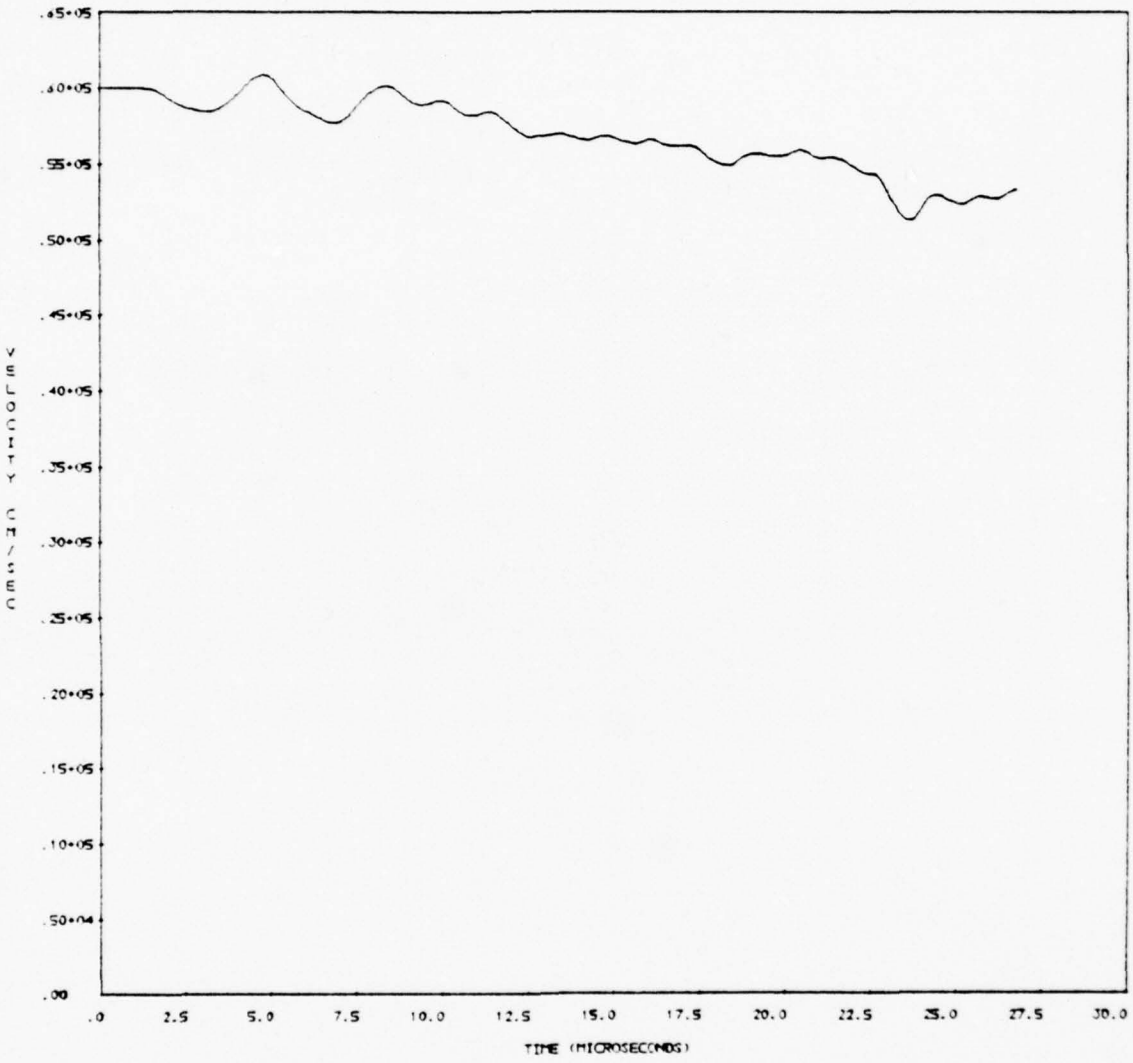

Figure 12. Axial velocity history at Gage 3.

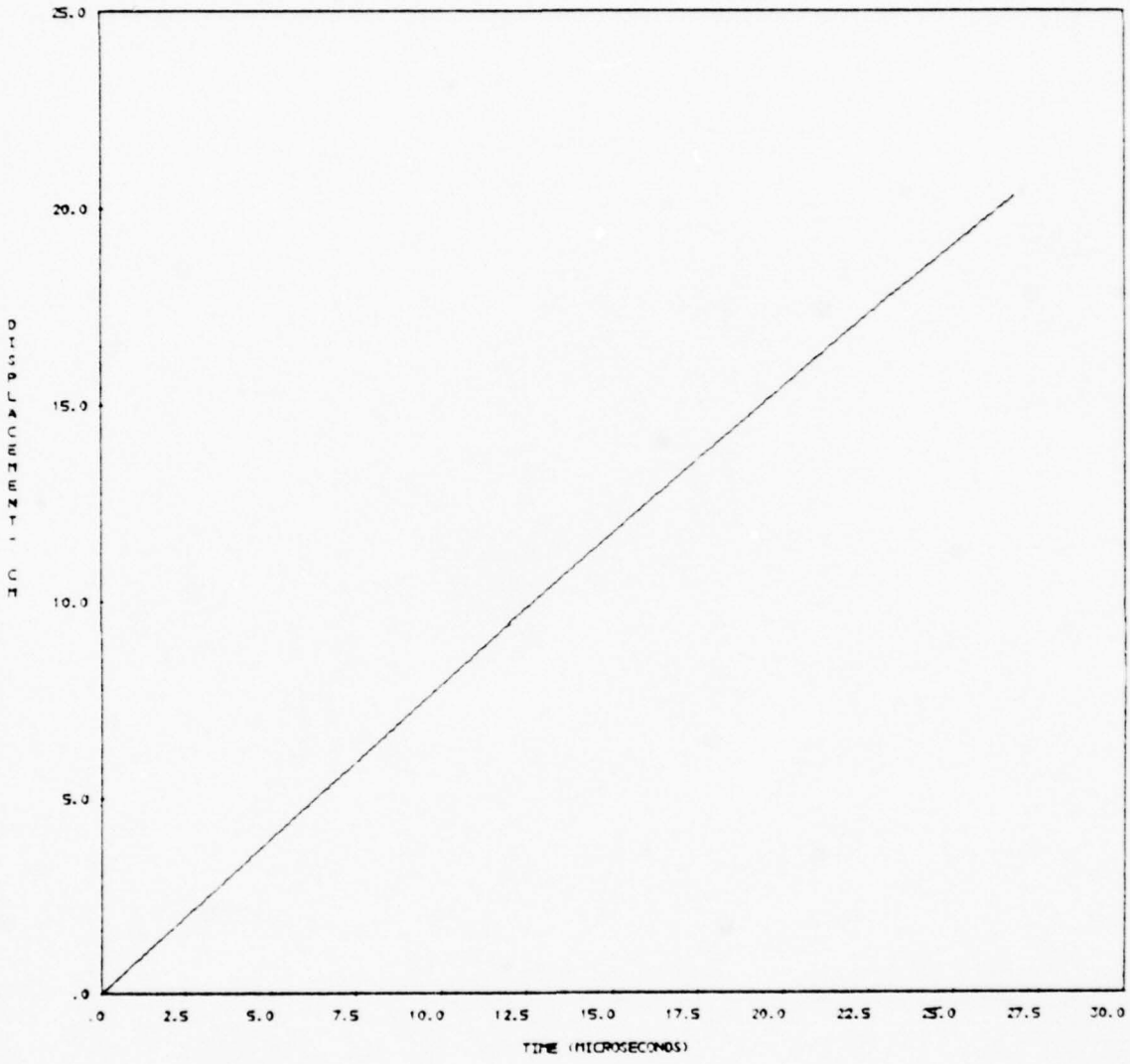

Figure 13. Axial displacement history at Gage 3.

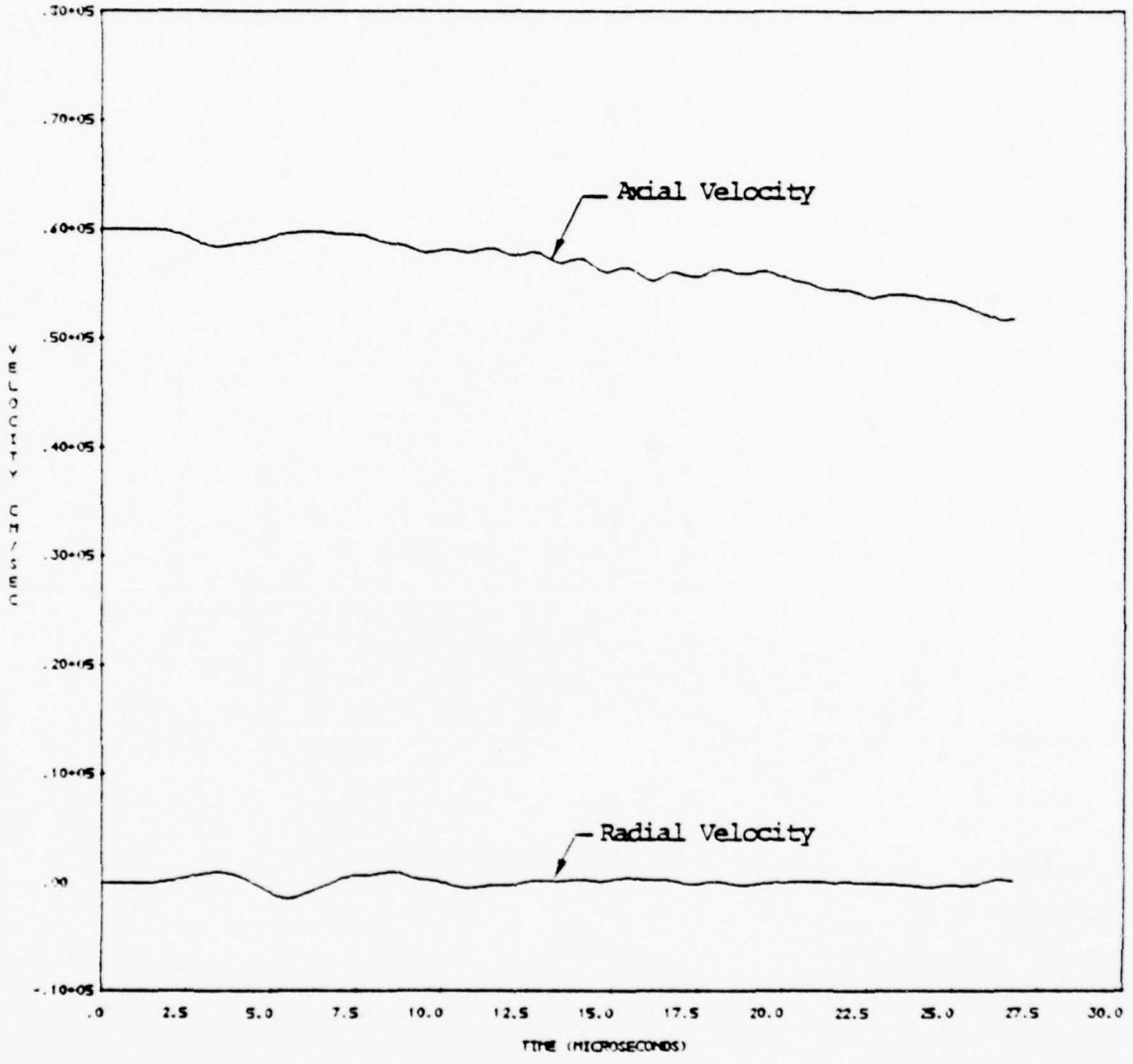

Figure 14. Velocity histories at Gage 4

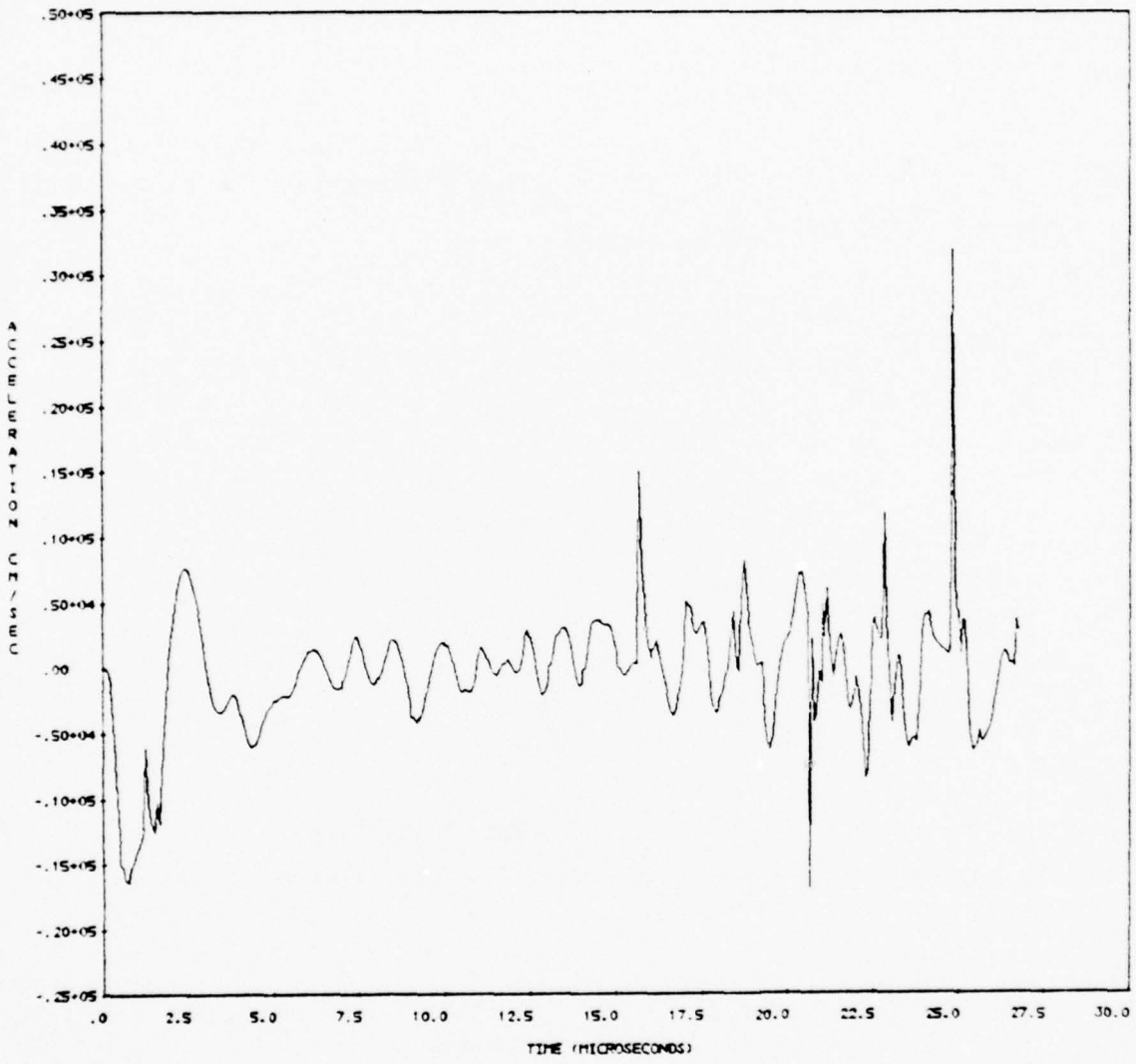

Figure 15. Axial acceleration history at Gage 5.

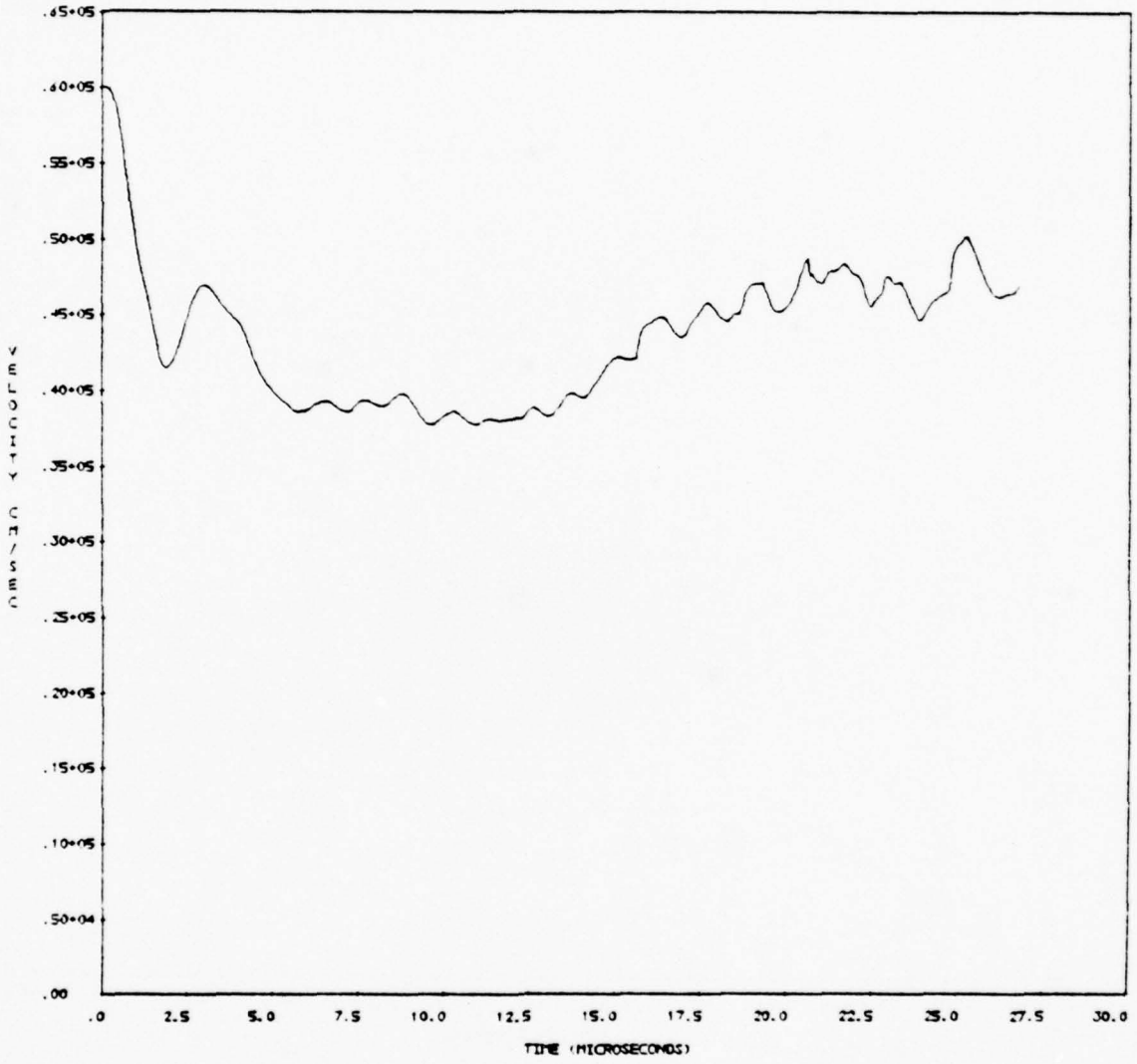

Figure 16. Axial velocity history at Gage 5.

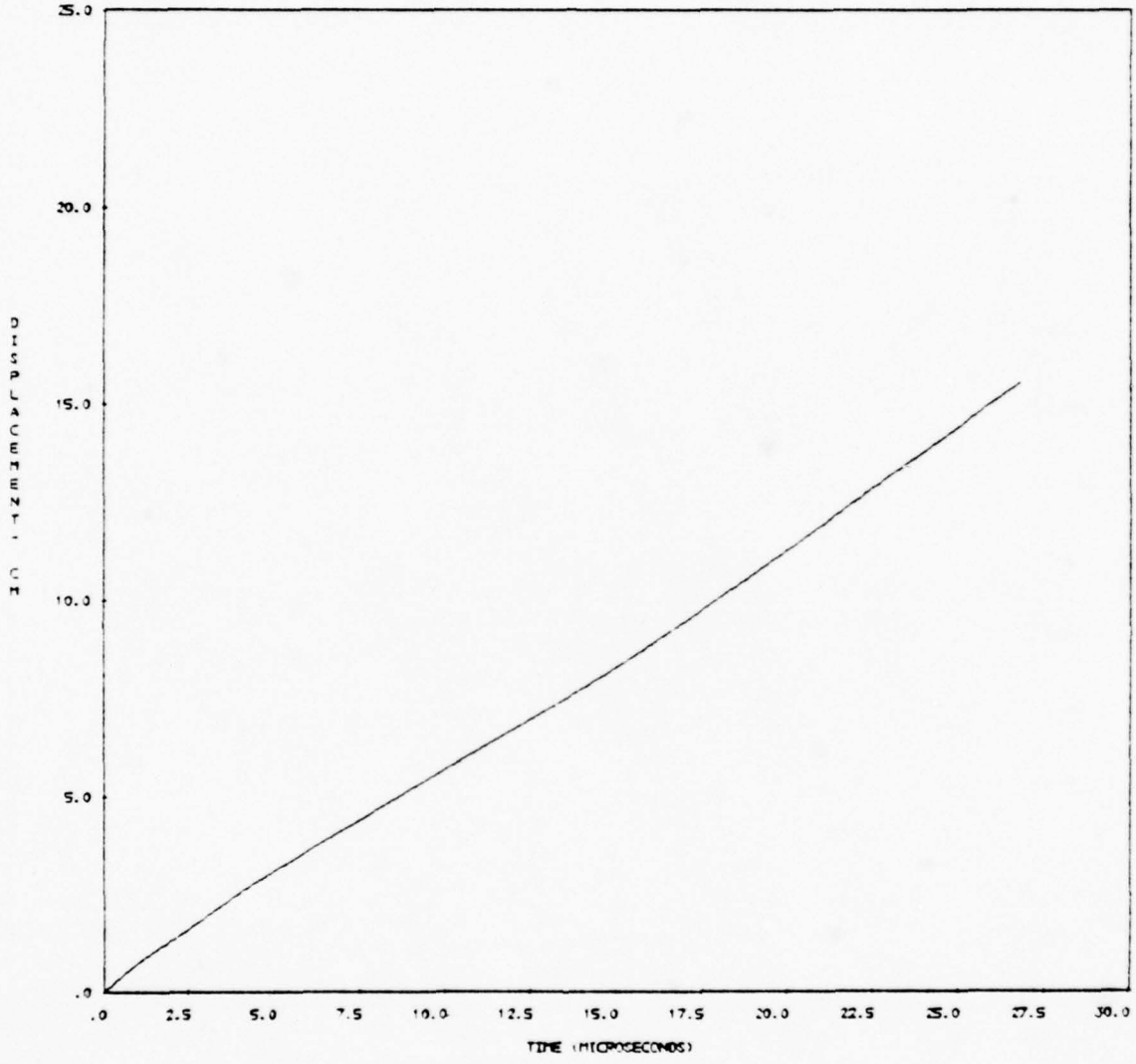

Figure 17. Axial displacement history at Gage 5.

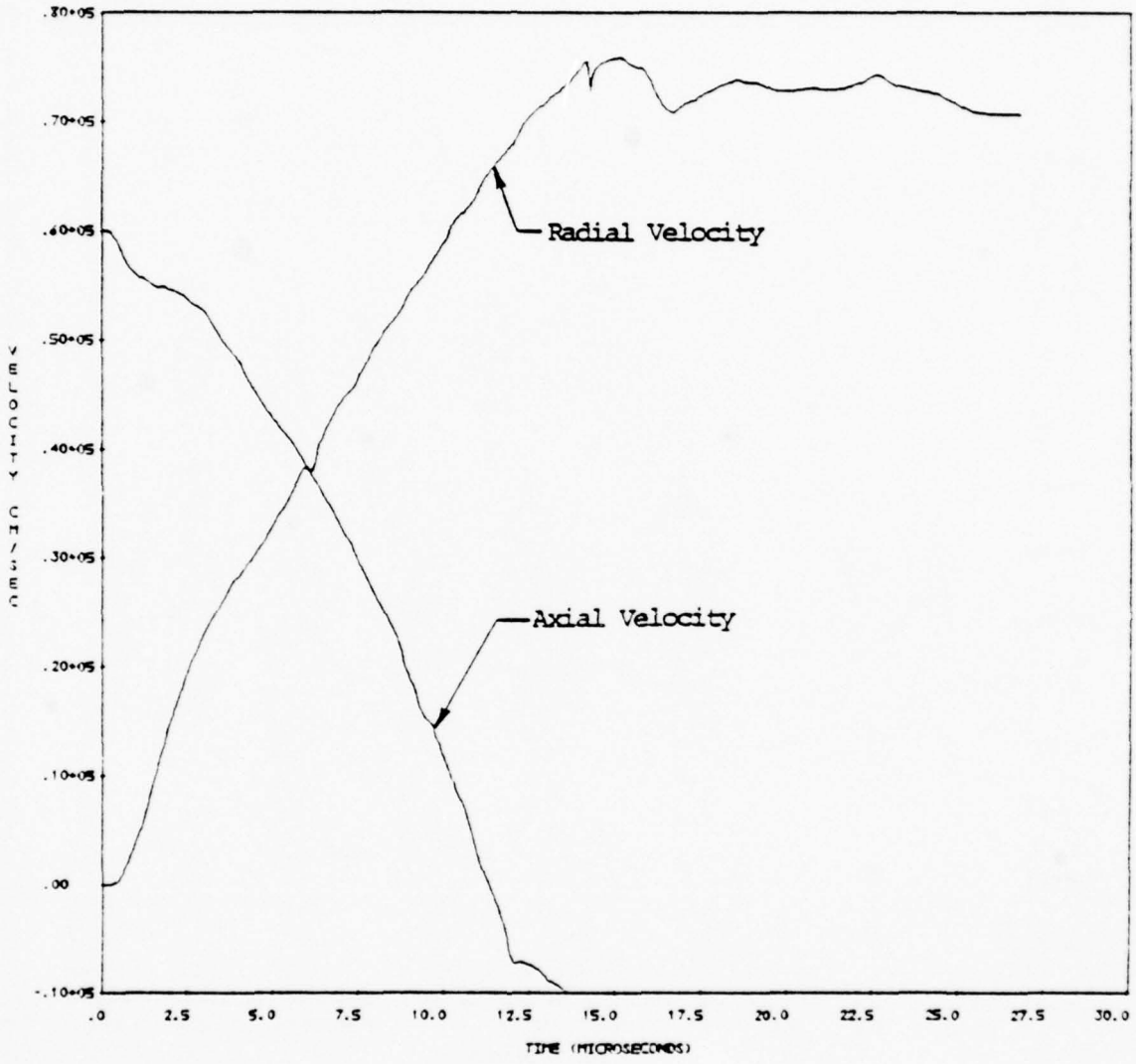

Figure 18. Velocity histories at Gage 6.

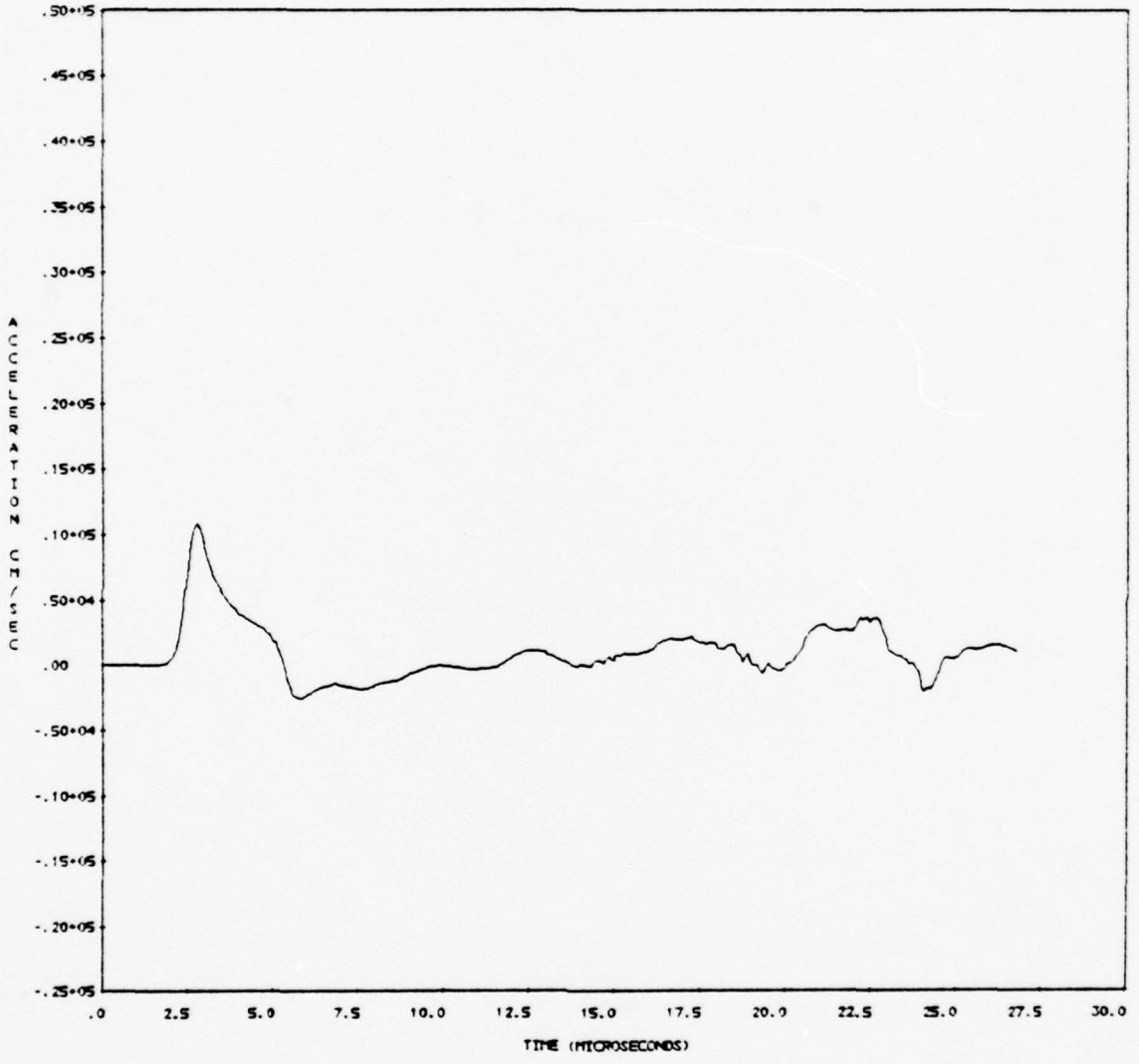

Figure 19. Axial acceleration history at Gage 7

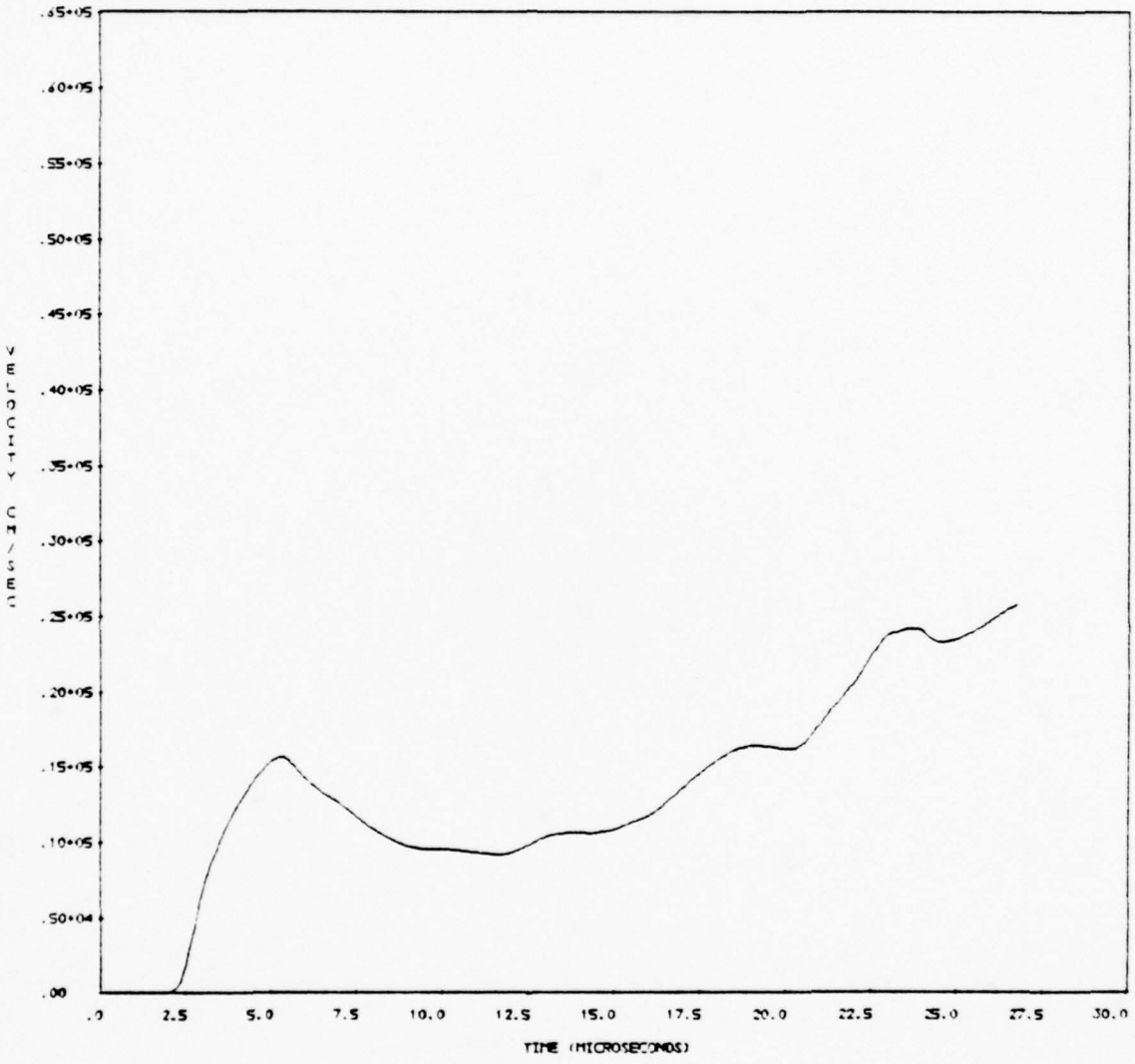

Figure 20. Axial velocity history at Gage 7.

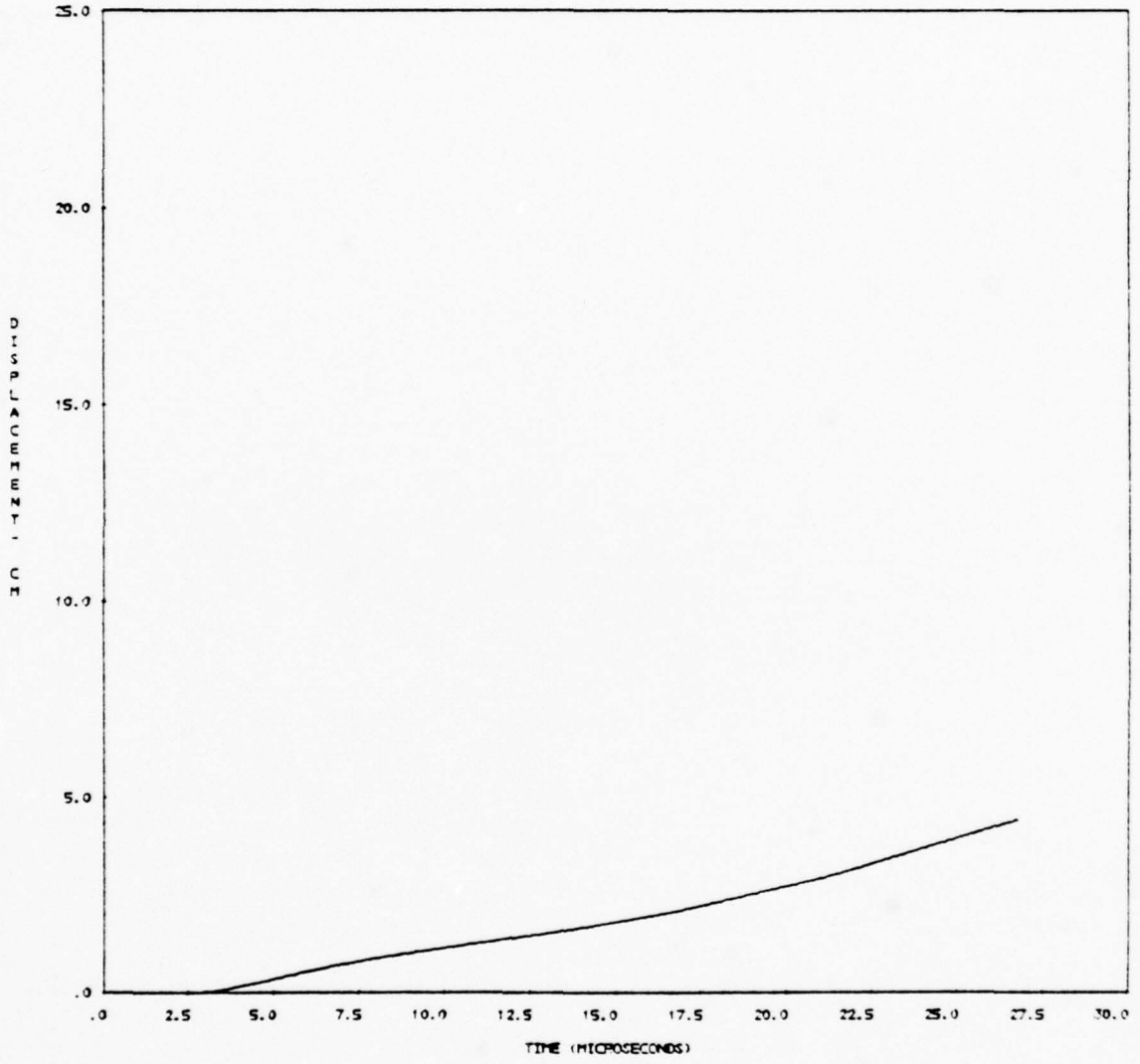

Figure 21. Axial displacement history at Gage 7.

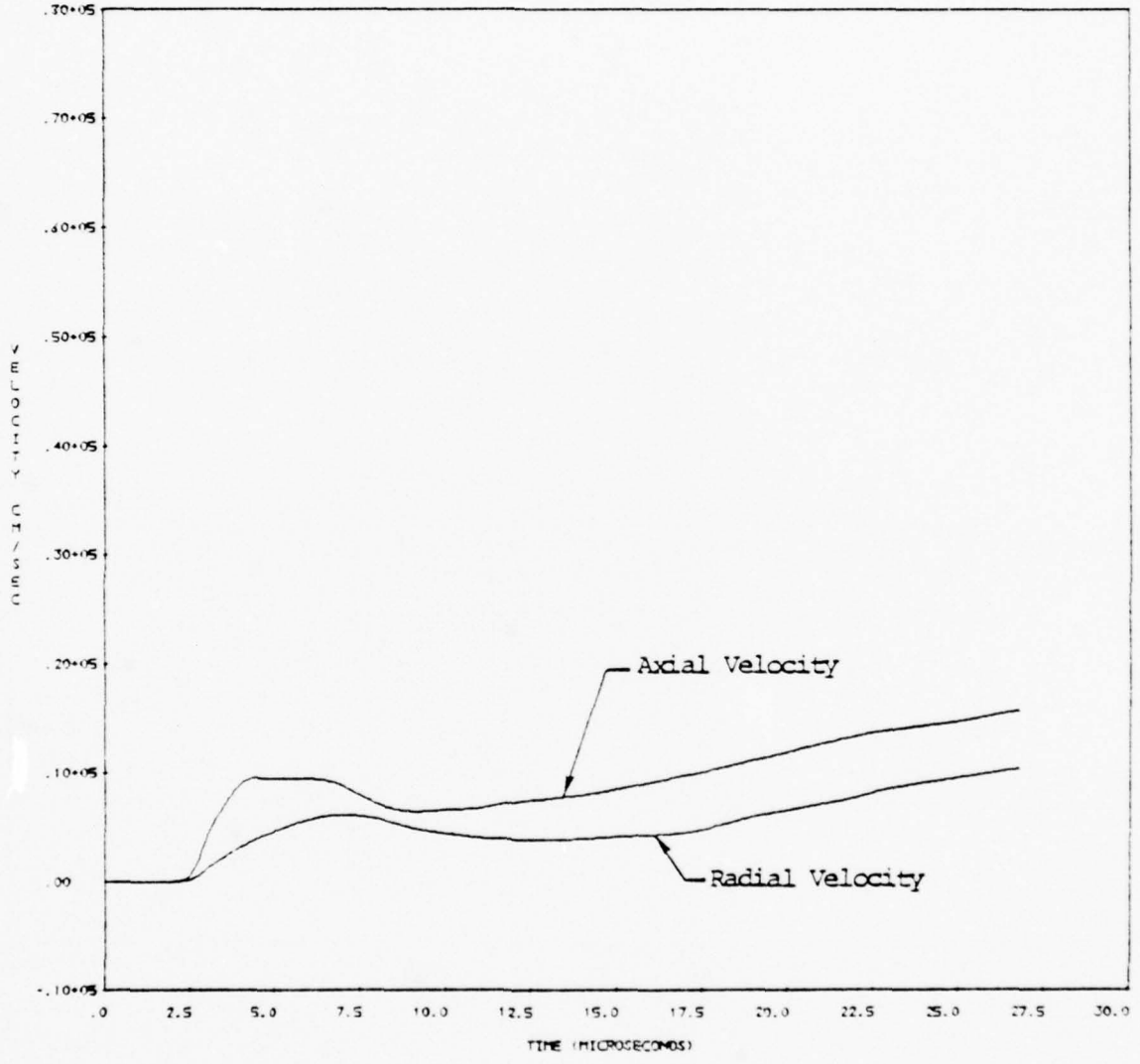

Figure 22. Velocity histories at Gage 8.

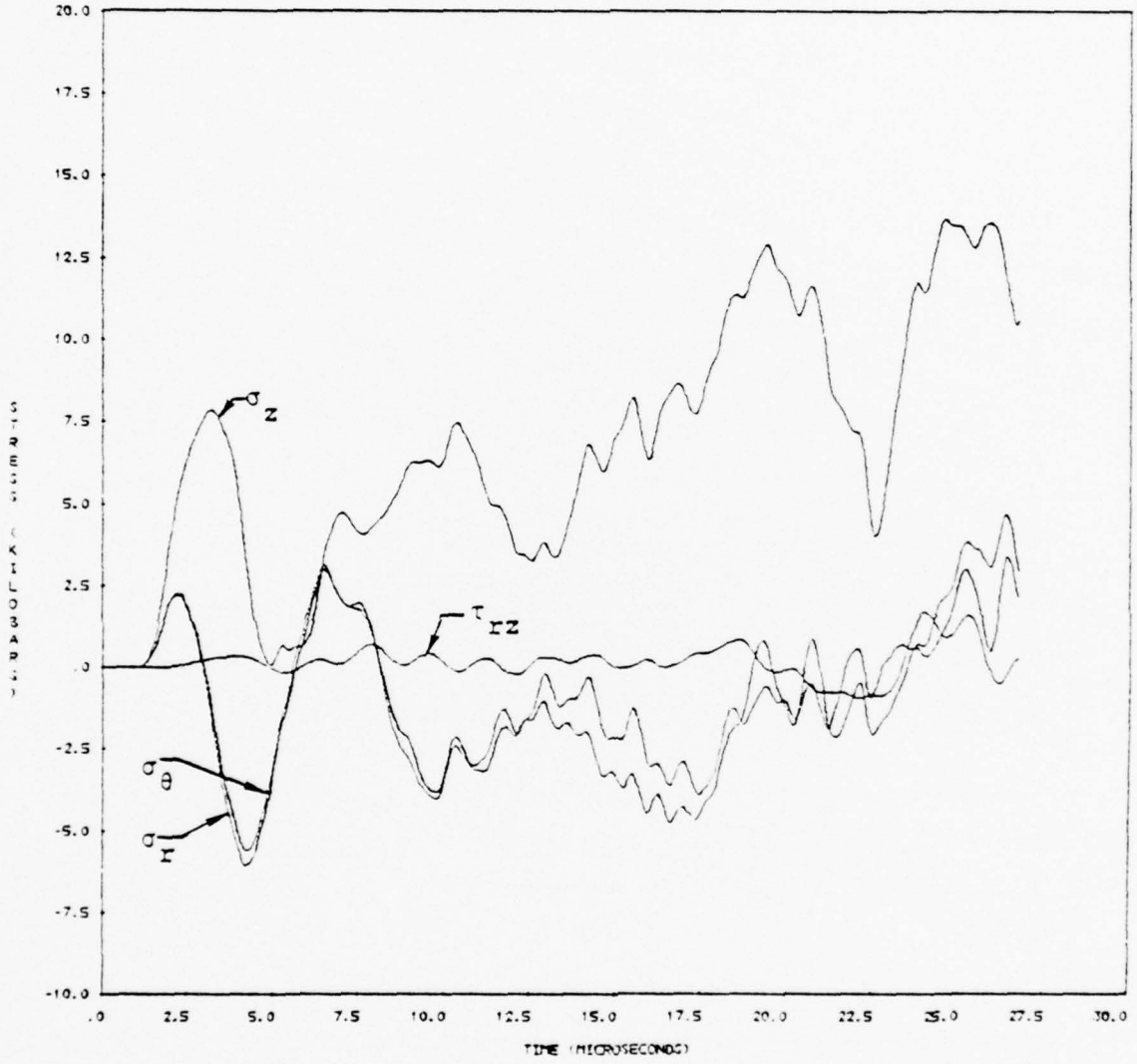

Figure 23. Stress histories at Gage 3.

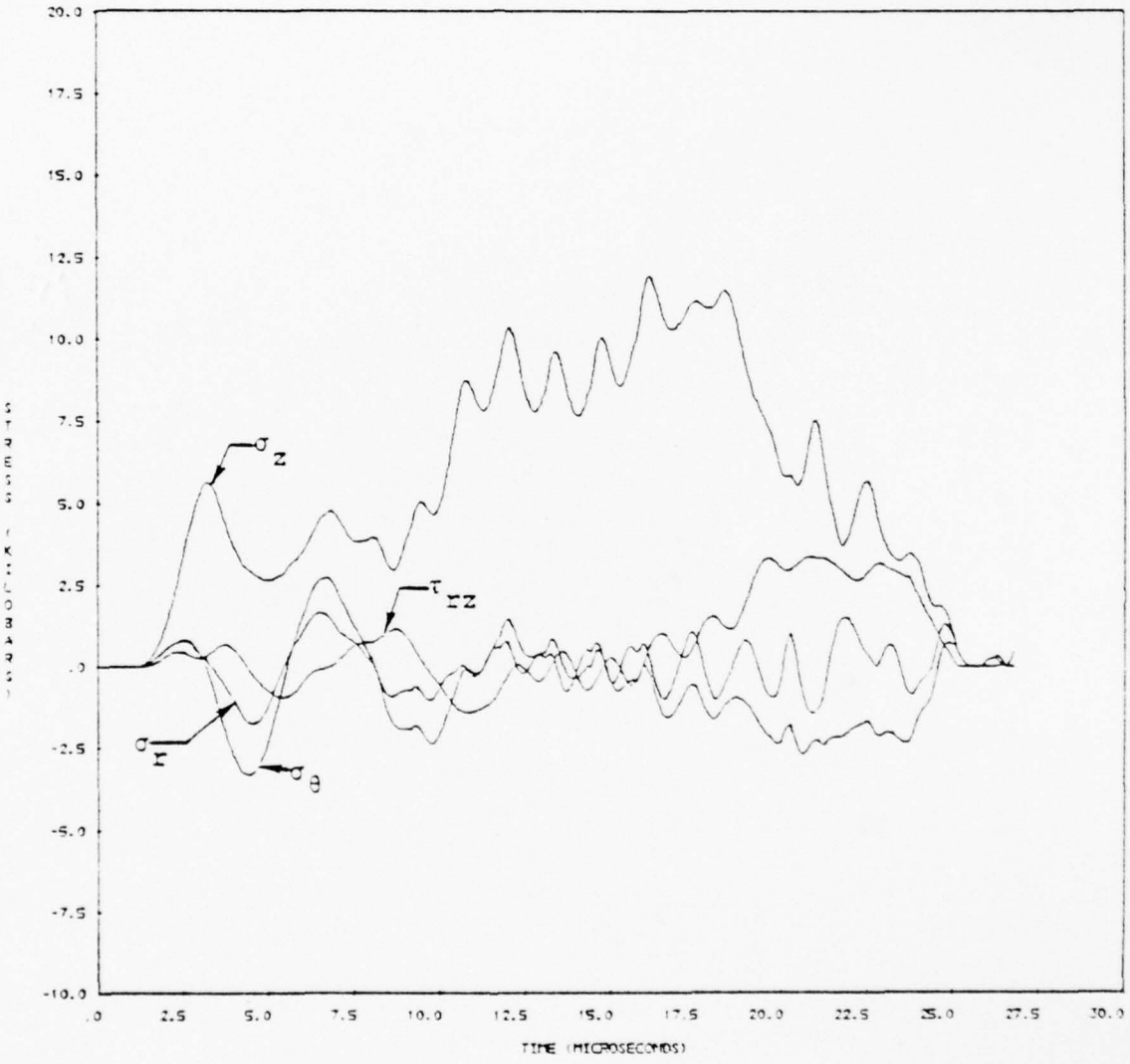

Figure 24. Stress histories at Gage 4.

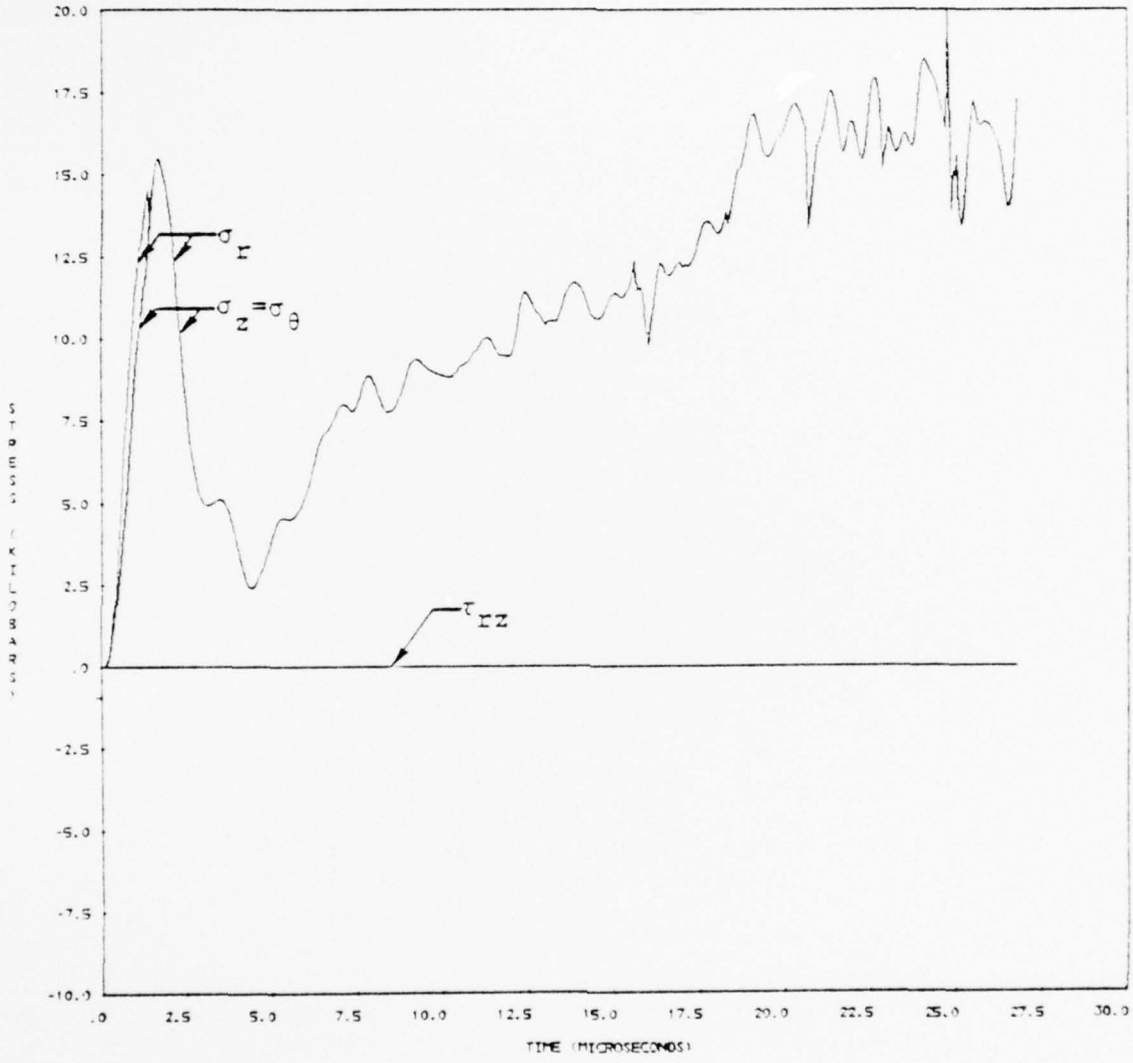

Figure 25. Stress histories at Gage 5.

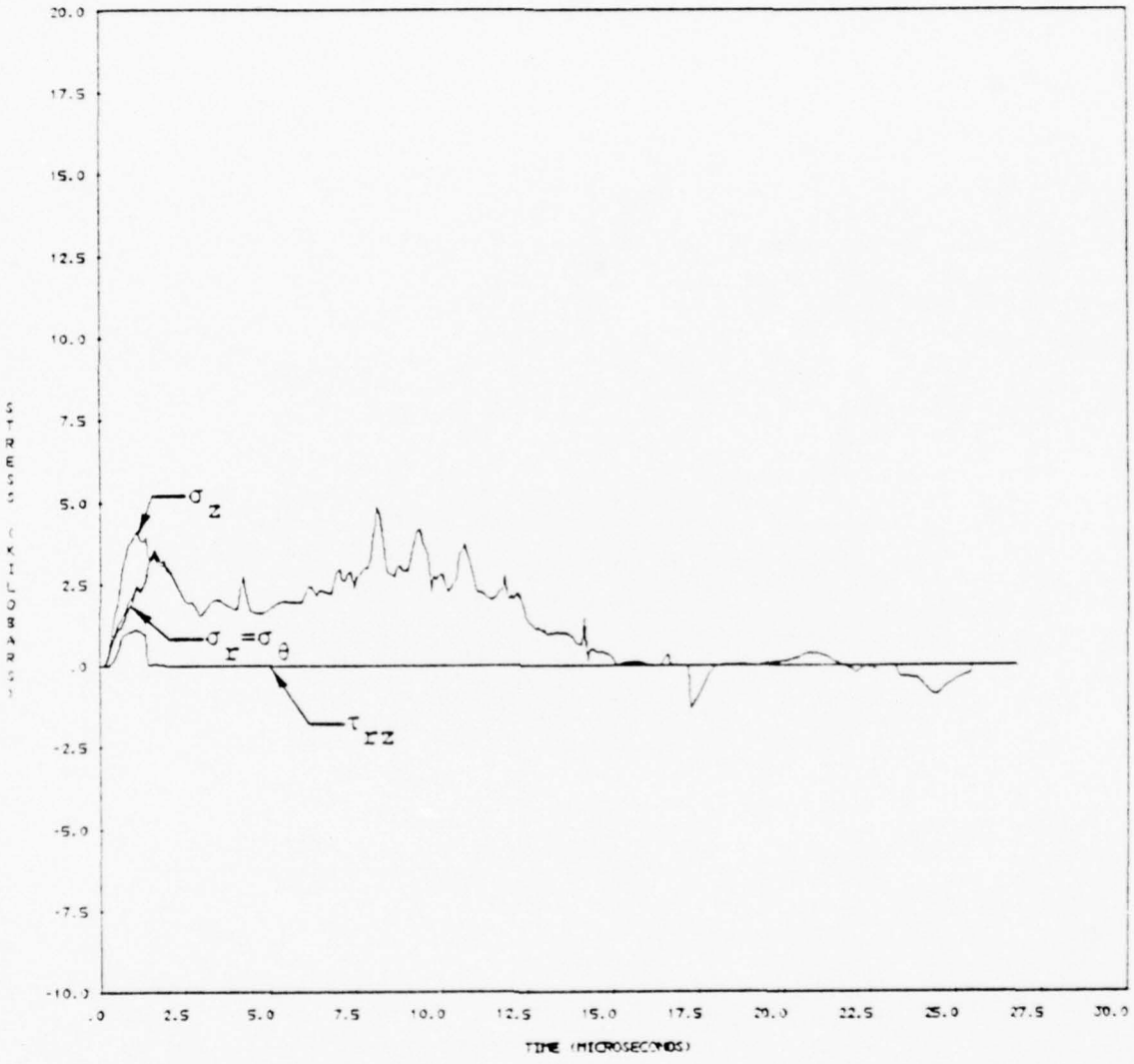

Figure 26. Stress histories at Gage 6.

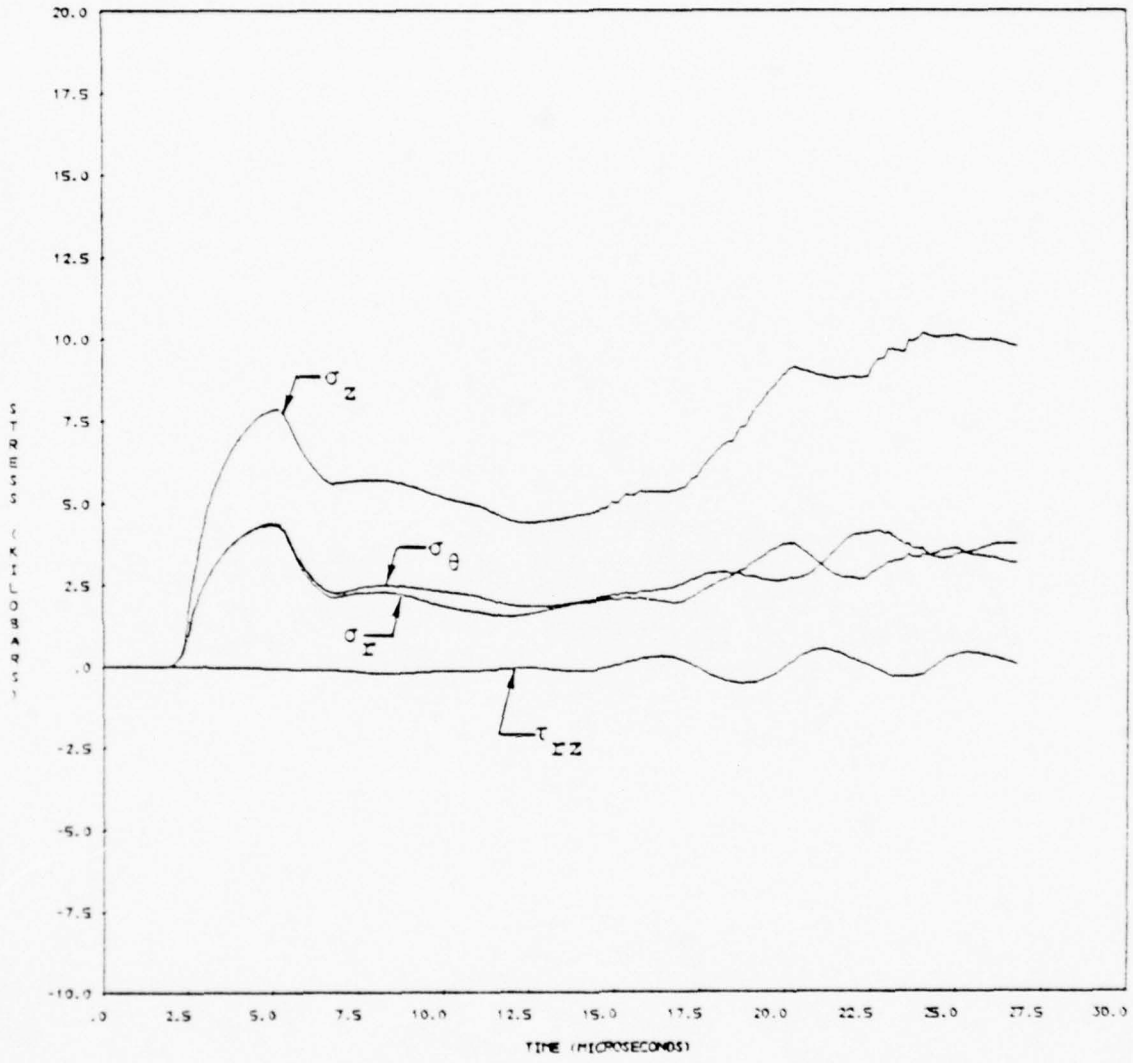

Figure 27. Stress histories at Gage 7.

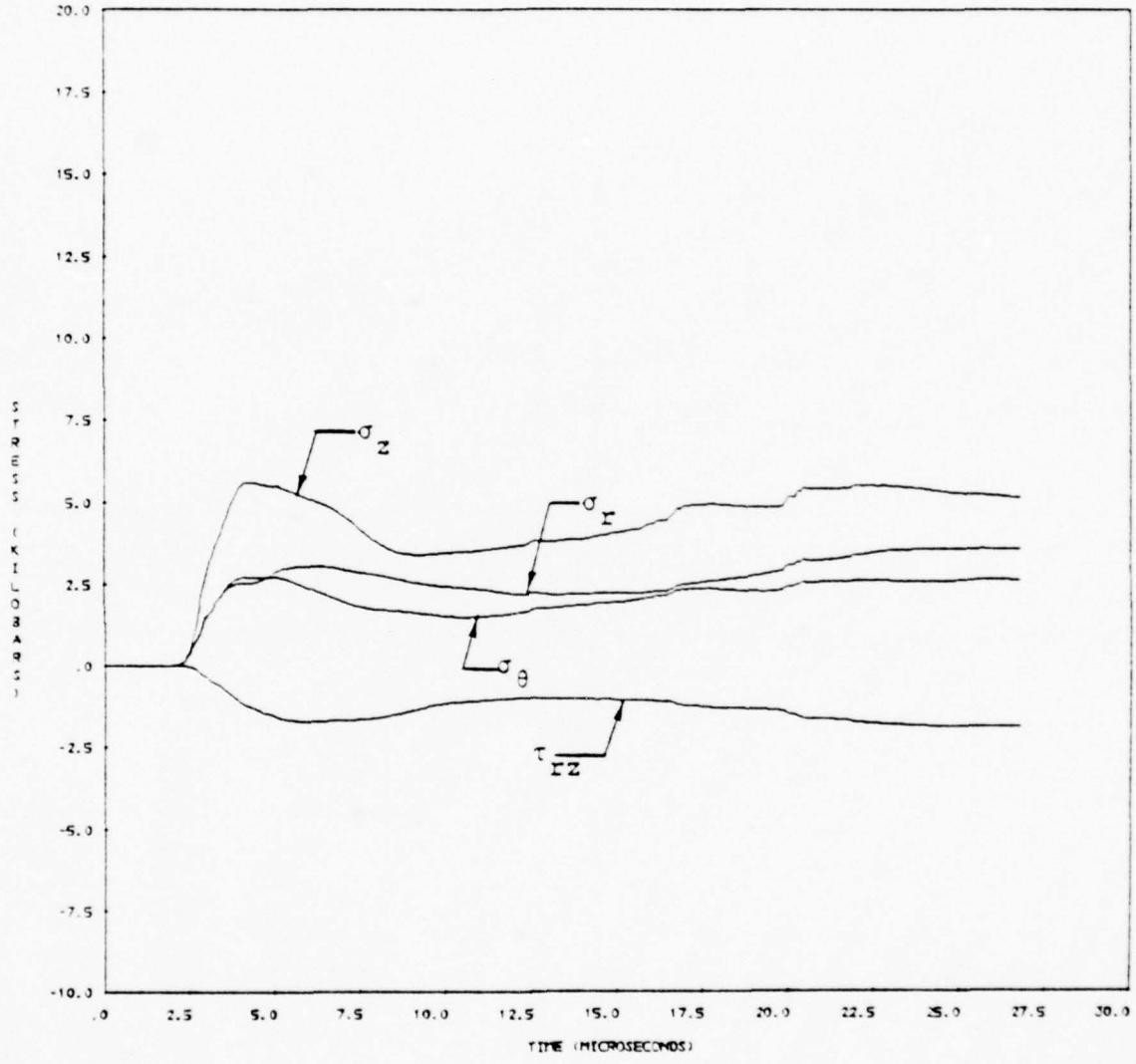

Figure 28. Stress histories at Gage 8.

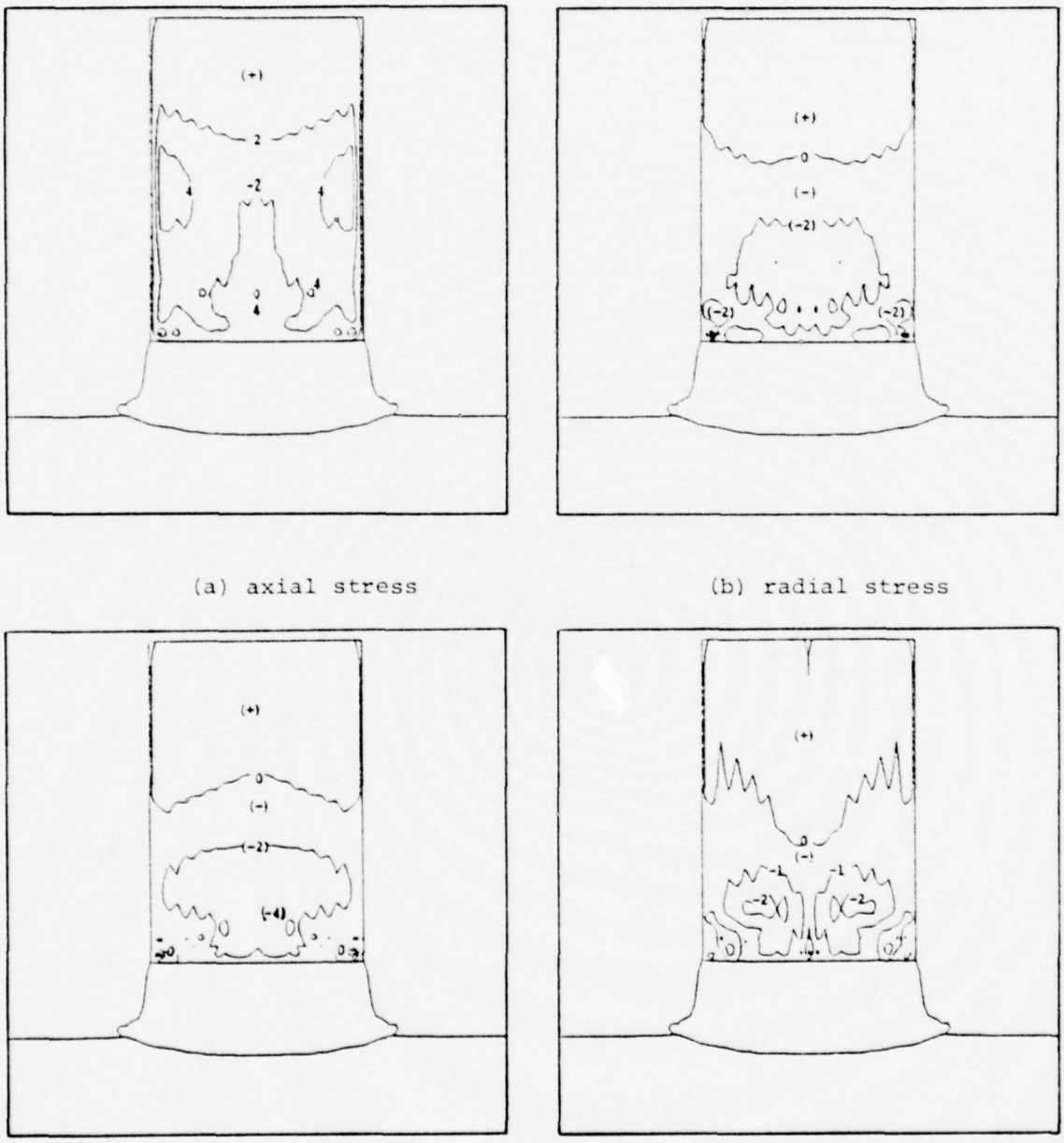

(a) axial stress

(b) radial stress

(c) hoop stress

(d) shear stress

Figure 29. Stress contours in steel body at 5 μsec.

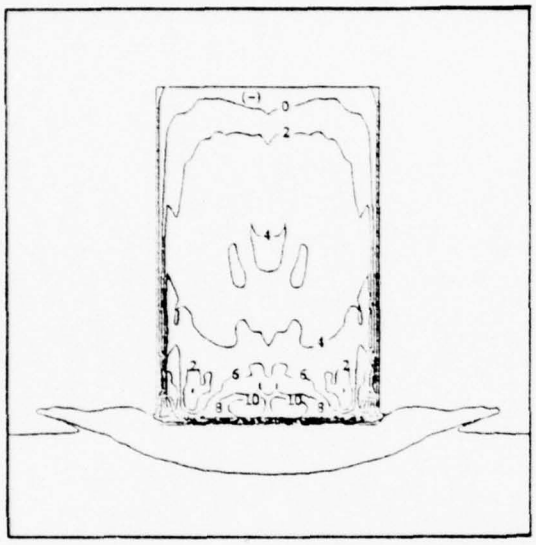

(a) axial stress

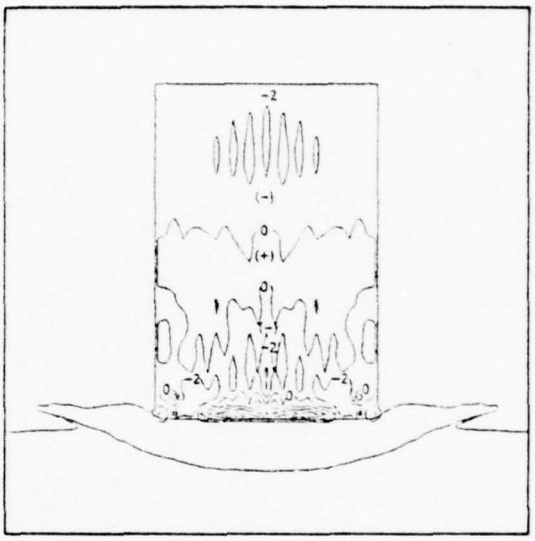

(b) radial stress

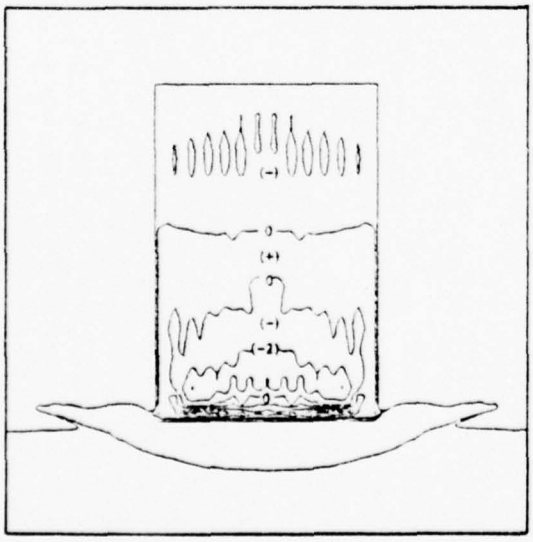

(c) hoop stress

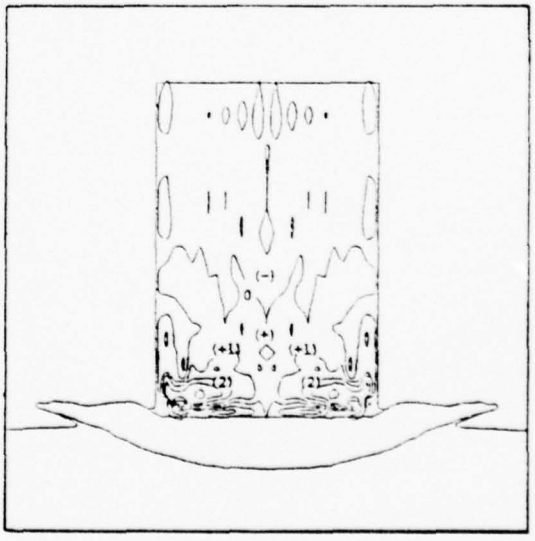

(d) shear stress

Figure 30. Stress contours in steel body at 15 μsec.

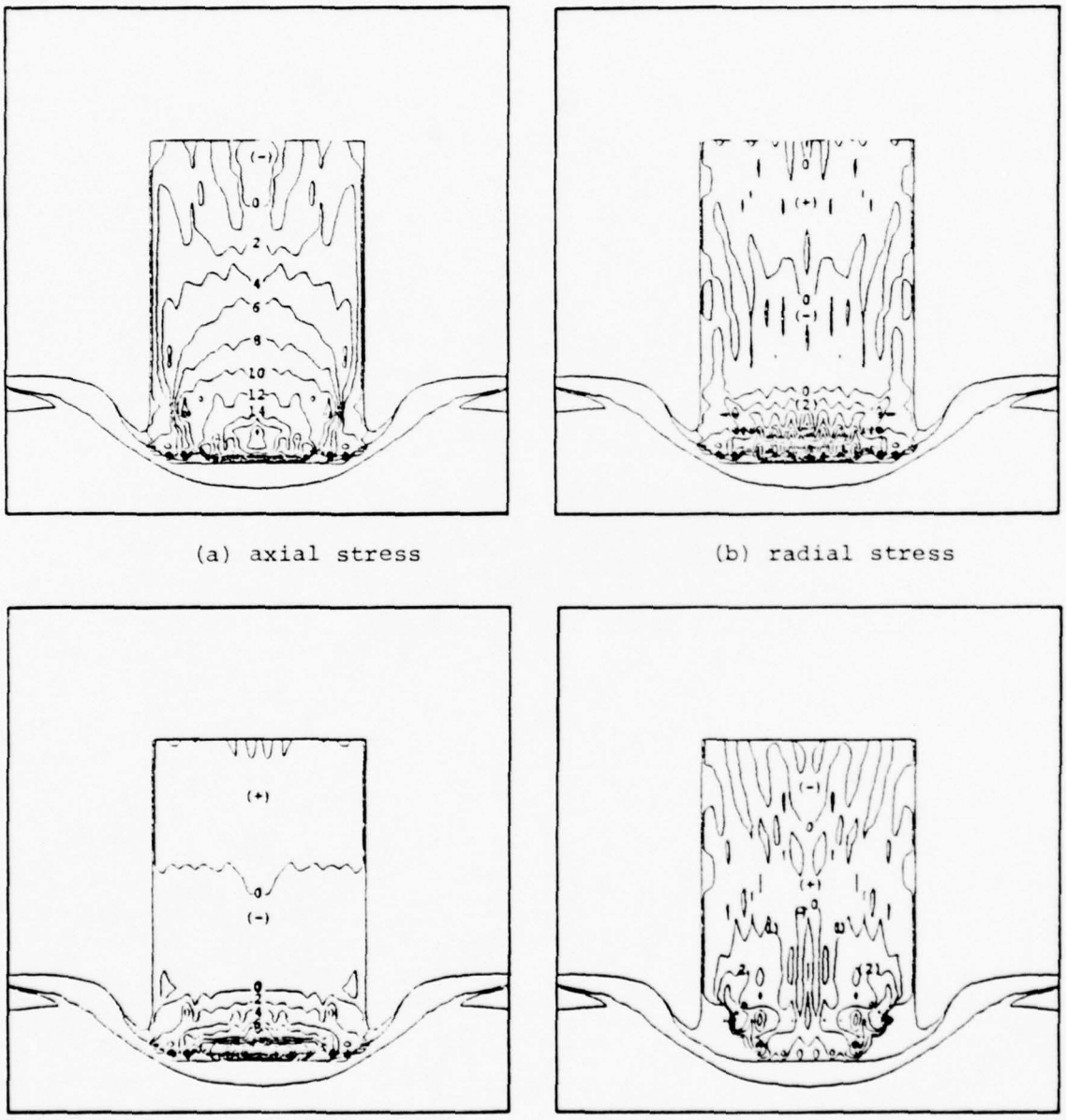

(a) axial stress

(b) radial stress

(c) hoop stress

(d) shear stress

Figure 31. Stress contours in steel body at 25 μsec.

5. CONCLUSIONS

The study reported herein should be regarded as an initial attempt to develop a numerical method suitable for analyses of problems involving the impact of nose-capped projectiles with rock. Such problems are characterized by large plastic deformation, extensive material failure, frictional sliding between cracked (comminuted) rock and the projectiles metal surfaces, and systems involving multiple materials.

In view of the complexities noted above, neither the standard Eulerian nor the standard Lagrangian approaches are well-suited for numerical analysis of such problems. A decision was made at the beginning of the effort to adopt the Eulerian approach as the basis on which to develop a numerical method for this class of problem; this decision was difficult and made only after weighing the many advantages and disadvantages of both approaches. The Eulerian approach appeared to offer more promise primarily because of its superior ability to deal with large deformations, which we felt to be important in the analysis of highly deformable projectiles. Lagrangian methods are nevertheless frequently applied by the defense community to problems involving large deformations, and numerical solutions are made possible through extensive rezoning procedures. Little can be said, however, about the credibility (accuracy) of results so obtained.

The main objectives of this study were accomplished, namely (a) a new Eulerian code CAPRI was developed which is specifically tailored to treat problems involving the normal impact of deformable projectiles with rock, and (b) the application of CAPRI to a projectile-rock impact problem was demonstrated.

The CAPRI code is a two-dimensional Eulerian code developed from the existing HELP code[8] framework. It features the following new capabilities which are evidently important for the class of impact problems of interest to the present investigation.

- Accounts for material strength in mixed-material computational cells.
- Treats frictional sliding between material surfaces in contact.
- Attempts to satisfy the correct boundary conditions on stress and velocity at interfaces between materials in contact.
- Contains an improved algorithm for transporting mass and other related material properties through the Eulerian grid.
- Accommodates complex geologic material models, including those having a number of history-dependent parameters (see Appendix A for further discussion on this point).

The major portion of study was devoted to the formulation, development and debugging of the intricate numerical algorithms required to incorporate the features listed above.

To examine and demonstrate the ability of the new code CAPRI to perform numerical analysis of deformable projectile-rock impacts, it was applied to a problem involving a solid cylindrical projectile, having a soft magnesium nose cape, impacting sandstone at normal incidence. A numerical solution, which appears to be acceptable, was obtained out to a time after impact (27 μsec) at which a substantial part of the penetration process had occurred. In the process of performing this calculation, however, a number of difficulties with the numerical scheme arose which made it impossible to continue the calculation until the source of the difficulty was uncovered. An appropriate modification was made in the flow field at that time, and the calculation was resumed. As noted earlier, however, the modifications were of limited extent and made in material regions where their effects were probably of negligible significance.

The calculation was not continued beyond 27 μsec because, by this time, the soft magnesium nose cap material had undergone such severe plastic flow that its thickness, in some region became less than the Eulerian zone size; this resulted in three materials being present in one zone and, in the present state of development, CAPRI is unable to adequately cope with such a situation. The calculation could have been continued further by rezoning the calculational field with smaller Eulerian zones; this, however, would provide only a temporary solution if further thinning of the magnesium layer reduced its thickness to that of the new zone size. Two other alternatives appear to be more desirable, namely, either generalize the numerical scheme to handle (admittedly approximate) three materials in a cell, or in very thin magnesium regions remove the magnesium and reposition the sandstone interface to be in immediate contact with the steel.

Some general comments on the study are as follows:

(1) No firm conclusion can be drawn from the study reported here regarding the effectiveness of nose caps in reducing the level of stress propagated back into the main body of a projectile impacting rock. To address this question, numerical calculations should be performed with the CAPRI code for projectiles having (a) no nose cap and (b) nose caps of material harder than the steel main body, say a tungsten alloy. On the basis of one-dimensional response considerations presented in Section 3.3, however, it was found that the use of a soft nose cap served to increase the level of stress propagated into the main steel body. Conversely, the use of a nose cap of material harder than steel serves to reduce the transmitted stress level. The validity of these conclusions, based on one-dimensional considerations, needs to be investigated under more general two-dimensional conditions.

(2) The numerical approach developed and incorporated in CAPRI for treating frictional sliding between materials appears to be reasonably accurate so long as the volumes of the two sliding materials in a mixed cell are approximately of the same order of magnitude. However, as the sliding interface moves through the fixed Eulerian grid during the calculation, situations will frequently arise wherein the volume of one material is very much less than that of the other. As the relative volume of one of these materials decreases, the accuracy of the present numerical algorithm for treating the motion of the smaller volume material also decreases. This may not, however, cause a significant problem since a numerical error made in a small volume of material would be expected to have much less effect on the overall response of the projectile-rock system than a comparable error made in a larger volume of material.

(3) It is not clear from the results of the present study that the additional complexity introduced into the CAPRI code by the incorporation of the sliding friction capability is justified, since the levels of shear stress generated by high speed sliding between steel and rock are evidently relatively small. The frictional sliding law adopted in the calculation presented herein was suggested to us by Dr. Paul Hadala, U.S. Army Waterways Experiment Station, on the basis of results from a related experimental study.[10] According to this law, the peak shear stress that can be generated from frictional sliding is about 0.1 kbars and, for the range of normal stresses of major interest, the shear stress is expected to be considerably less than 0.1 kbars. It is not clear what influence such relatively small shear stresses have on (a) the nose cap deformation and (b) the overall projectile deceleration. If their effect is small and can be reasonably neglected, it would provide considerable simplification in the numerical scheme; this was not investigated, however, in the present study.

(4) The ability of the CAPRI code to treat problems involving the impact of highly deformable projectiles with rock was demonstrated for the case of a projectile that had a solid body. Although the scope of this study did not include analysis of several nose cap materials, a great deal can be learned about the effectiveness of various nose cap materials from analysis of nose capped solid projectiles. With the existing version of the CAPRI code, however, calculations can be performed for projectiles having shapes of more practical interest. Rather than the blunt nose type projectile considered in the present study, numerical studies should be performed for ogive-shaped projectiles having a variety of nose cap materials in order to fully understand the role that nose caps play in effecting stress levels transmitted into the main body of a projectile. Before such studies are undertaken, however, we recommend that some effort be devoted to improving several portions of the code.

REFERENCES

1. Triandafilidis, G.E., "State-of-the-Art of Earth Penetration Technology," The University of New Mexico, Albuquerque, DNA 4080F, May 1976.

2. Hadala, P.F., "Earth Penetration: FY 74 Results and FY 75 Activities," presentation at the DNA Strategic Structures Review Meeting held at Stanford Research Institute, Menlo Park, California February 1975.

3. Byers, R.K., A.J. Chabai and R.T. Walsh, "Predictions of Projectile Penetration Phenomena and Comparison with Experiments in a Soil Medium," Sandia Laboratories, Albuquerque, SAND 75-0174, October 1975.

4. Patterson, W.J., "DNA/Sandia Soil Penetration Experiment at DRES: Results and Analysis," Sandia Laboratories, Albuquerque, SAND-75-0001, October 1975.

5. Wagner, M.H., K.N. Kreyenhagen and W.S. Goerke, "Numerical Analysis of Projectile Impact and Deep Penetration into Earth Media," California Research and Technology, Woodland Hills, California, U.S. Army Waterways Experiment Station Report No. S-75-4, August, 1975.

6. Orphal, D.L., W.F. Borden, and J.E. Reaugh, "A Computation of a DNA Earth Penetration Experiment at the Watching Hill Site, DRES, Canada," Physics International Company, San Leandro, California, DNA-3685F, October 1975.

7. Yarrington, P., "Comparison of Calculations of Rigid and Deformable Projectiles Penetrating Soil," Sandia Laboratories, Albuquerque, SAND 76-0656, February 1977.

8. Wagner, M.H., C.C. Fulton and K.N. Kreyenhagen, "Finite-Difference Code Analyses of Earth Penetrator Dynamics in Rock Media," California Research and Technology, Report DNA 4069T, November 1976.

9. Hageman, L.J., D.E. Wilkins, R.T. Sedgwick and J.L. Waddell, "HELP: A Multi-Material Eulerian Program for Compressible Fluid and Elastic-Plastic Flows in Two Space Dimensions and Time," Systems, Science and Software, SSS-R-75-2654, July 1975.

10. Gaffney, E.S., "Measurements of Dynamic Friction Between Rock and Steel," Systems, Science and Software, SSS-R-77-3046, October 1976.

11. Wagner, M.H., "Material Model for Dakota Sandstone," California Research and Technology, Woodland Hills, California, January 1976.

12. Chabai, A.L., Memo on "Material Property Data for D6A-C Steel," Sandia Laboratories, Albuquerque, March 1974.

13. Metals Handbook, 8th Edition, Vol. 1, Properties and Selection of Metals, Edited by Taylor and Lyman, American Society for Metals, Metals Park, Ohio, 1961.

14. Butler, D.K., R.R. Nielsen, R.K. Dropek, and S.W. Butters, "Constitutive Property Investigations in Support of Full-Scale Penetration Tests in Dakota Sandstone, San Ysidro, New Mexico," U.S. Army Engineer Waterways Experiment Station, Technical Report S-77-3, April 1977.

15. Read, H.E., Letter to M. H. Wagner, CRT, dated June 24, 1976.

16. Wagner, M.H., Letter to H. E. Read, S^3, dated August 9, 1976.

APPENDIX A

COMPARISON BETWEEN LAGRANGIAN AND EULERIAN CODE CALCULATIONS FOR ONE-DIMENSIONAL WAVE PROPAGATION IN SANDSTONE

In order to examine how well the complex CRT sandstone model, with its six history-dependent parameters, can be treated by the Eulerian CAPRI code, a one-dimensional test problem involving wave propagation in sandstone was formulated[15] and numerically analyzed with both a Lagrangian code and an Eulerian code. The problem consisted of a sandstone flyer plate impacting a target of like material. The initial configuration of the system is shown in Figure 32. The impact velocity was chosen to be 3×10^4 cm/sec so that the impact stresses initially developed in the flyer and target would be about 8 kbars; at this stress level the deviatoric component of stress is a substantial part of the total stress, and it is not masked by a much larger hydrostatic component.

A uniform zone size of 0.05 cm was used in both the target and flyer plate. The calculation was taken out to 2.5×10^{-5} sec to permit the formation and subsequent propagation of the tensile wave the develops near the rear surface of the target; this permitted the code to exercise the tensile cutoff feature of the CRT sandstone model. However, no separation of the material was permitted in the calculation when the tensile cutoff was invoked.

At S^3's request, CRT performed a numerical analysis of the above problem with their Lagrangian WAVE-L code, to provide us with Lagrangian results against which we could compare the corresponding Eulerian CAPRI code results.[16] The results of the CRT numerical study are shown in Figures 33 to 37 where the calculated stress and generalized plastic strain fields at a

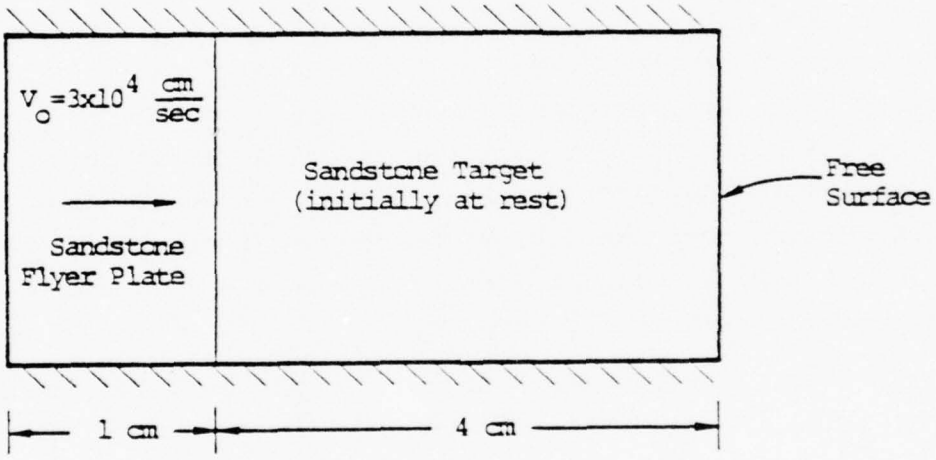

Figure 32. Initial configuration of one-dimensional impact test problem.

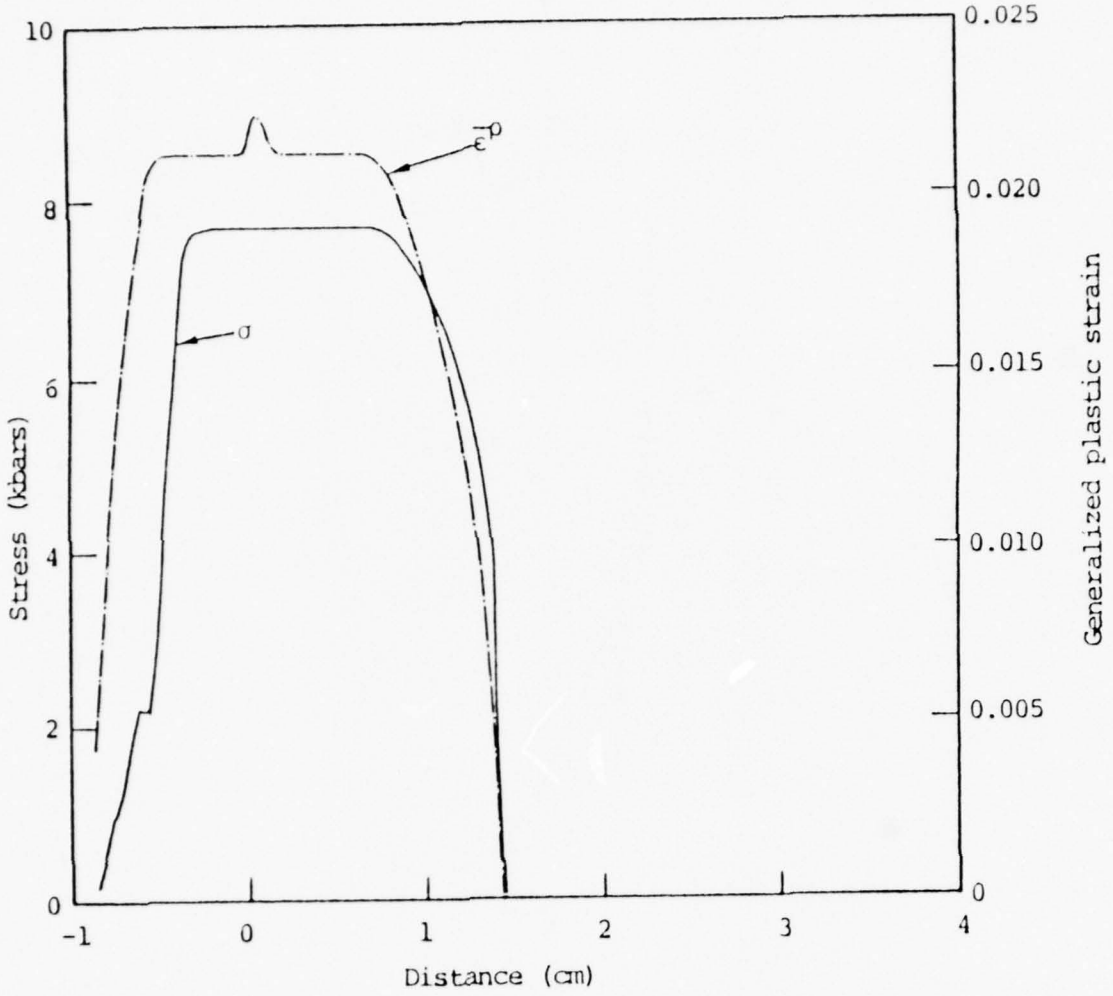

Figure 33. Stress and generalized plastic strain profiles at 5 μsec predicted by CRT Wave-L code.

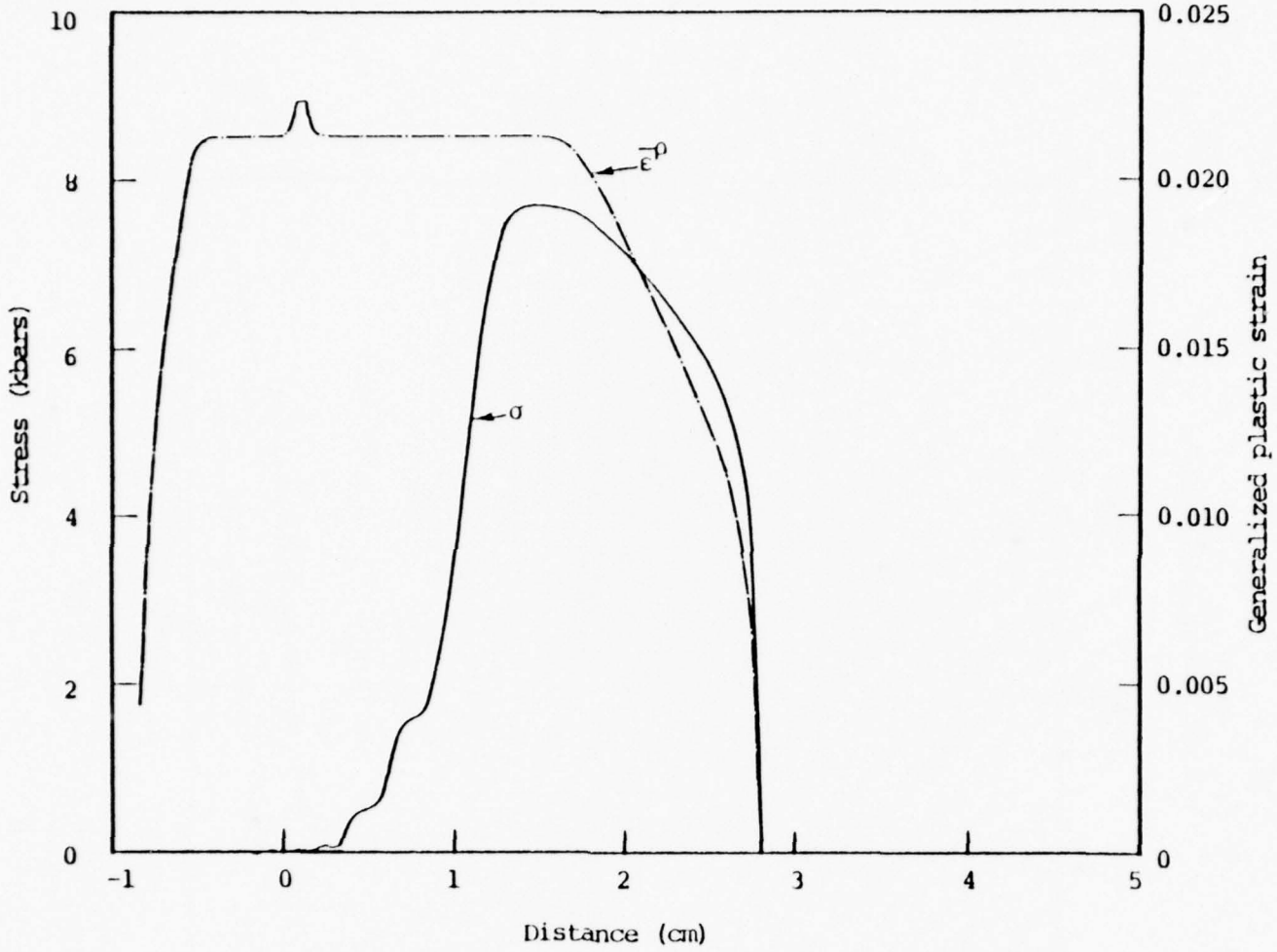

Figure 34. Stress and generalized plastic strain profiles at 10 μsec predicted by CRT Wave-L code.

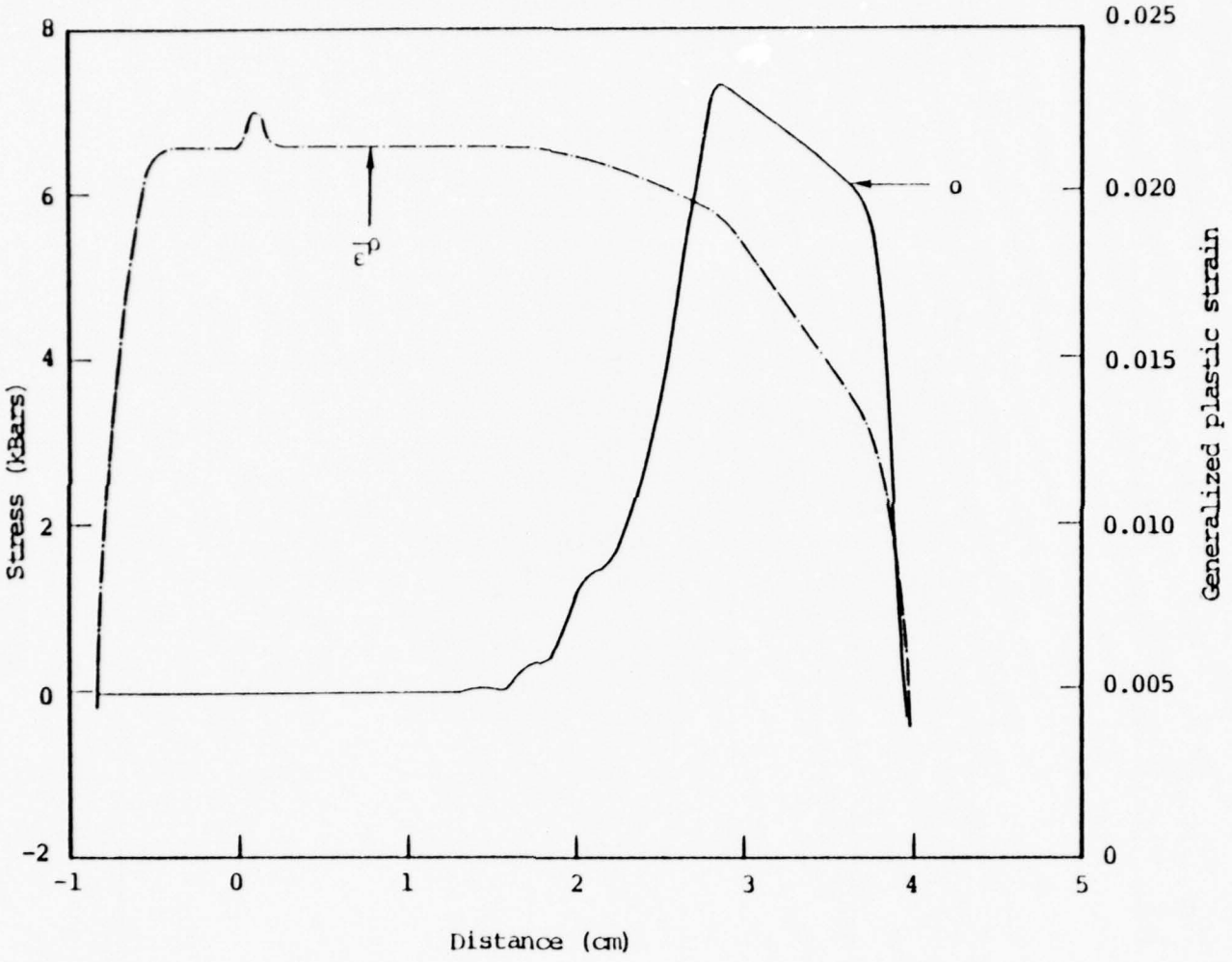

Figure 35. Stress and generalized plastic strain profiles at 15 μsec predicted by CRT Wave-L code.

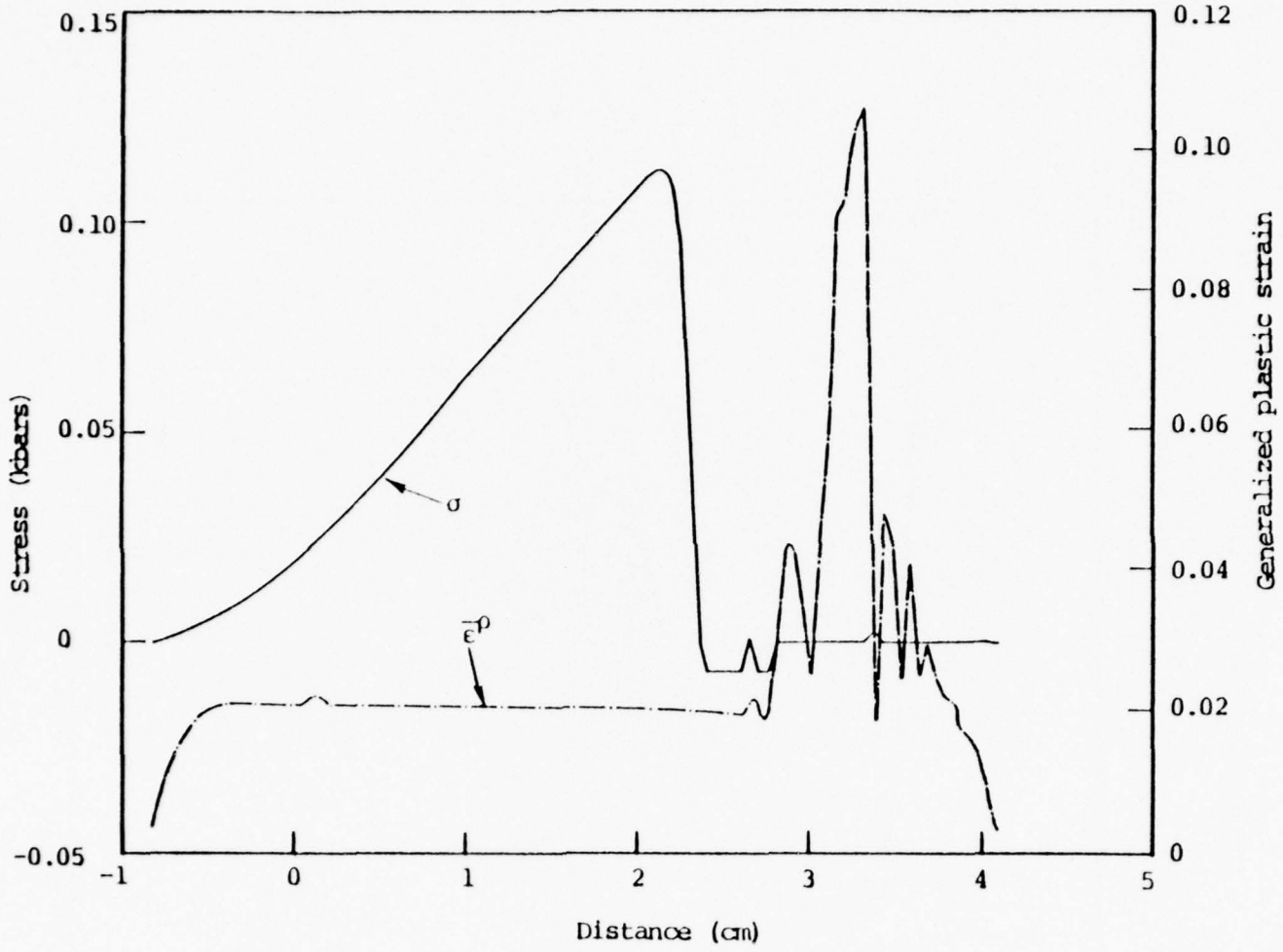

Figure 36. Stress and generalized plastic strain profiles at 20 μsec predicted by CRT Wave-L code.

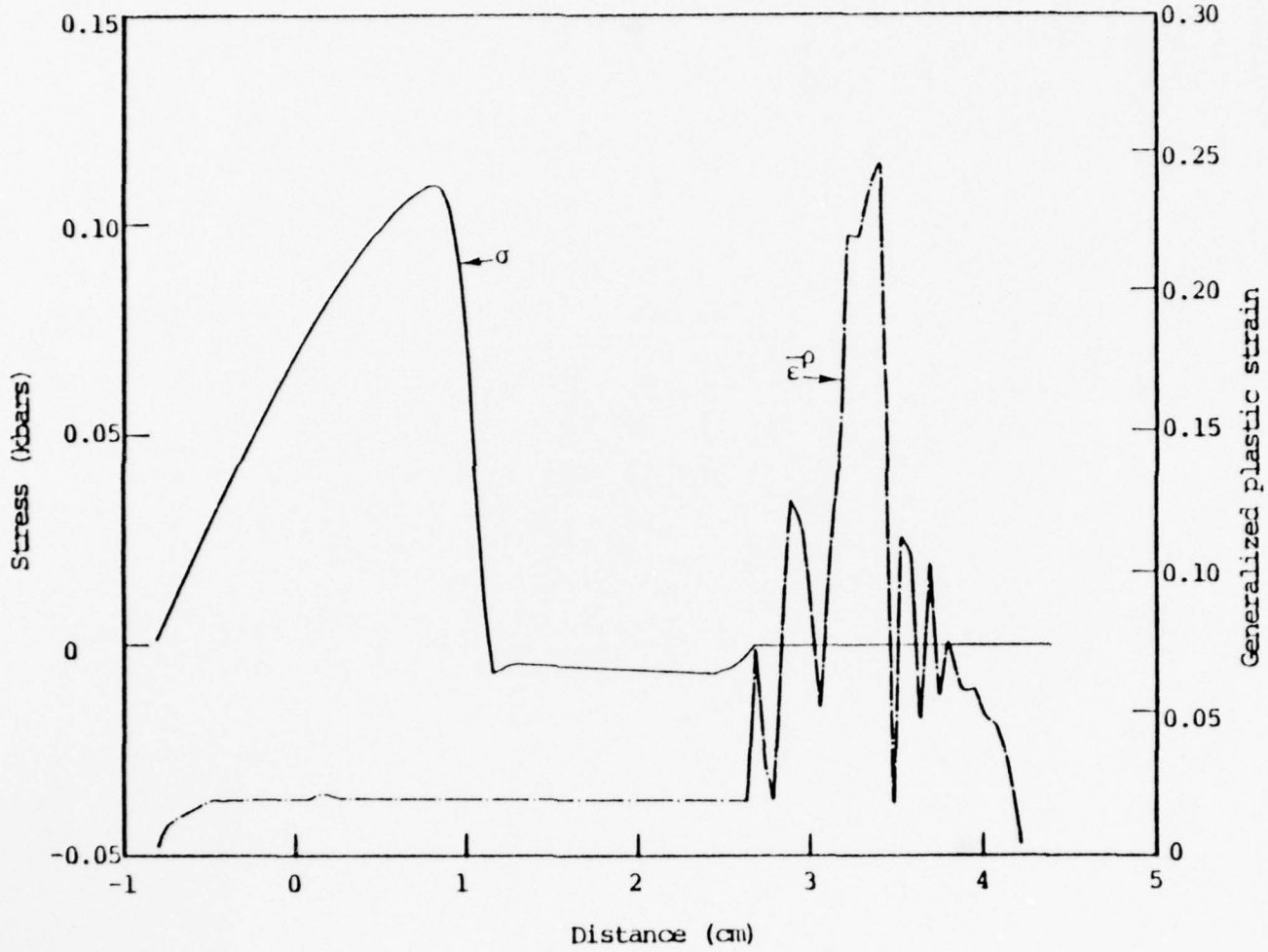

Figure 37. Stress and generalized plastic strain profiles at 25 μsec predicted by CRT Wave-L code.

number of selected times after impact are given. The results obtained by S^3 using the new Eulerian CAPRI code are depicted in Figures 38 to 42, where calculated stress and generalized plastic strain fields at the same times as the CRT results are shown. A comparison of the corresonding numerical solutions reveals that there is good agreement between the stress and generalized plastic strain fields predicted by the two different calculational approaches, and thus demonstrates that the spurious numerical diffusion of an Eulerian approach is not a serious factor, at least at these stress and velocity levels.

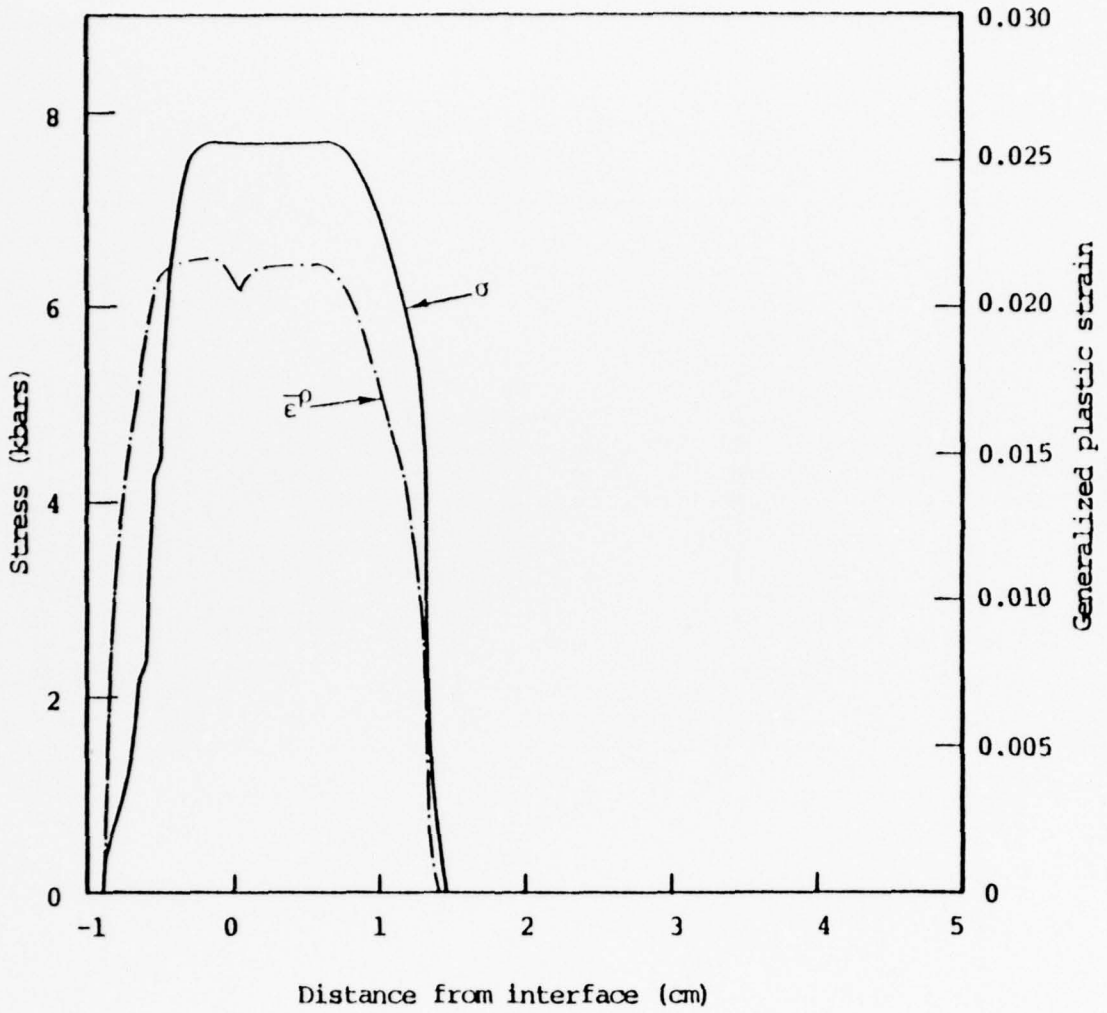

Figure 38. Stress and generalized plastic strain profile at 5 μsec predicted by CAPRI code.

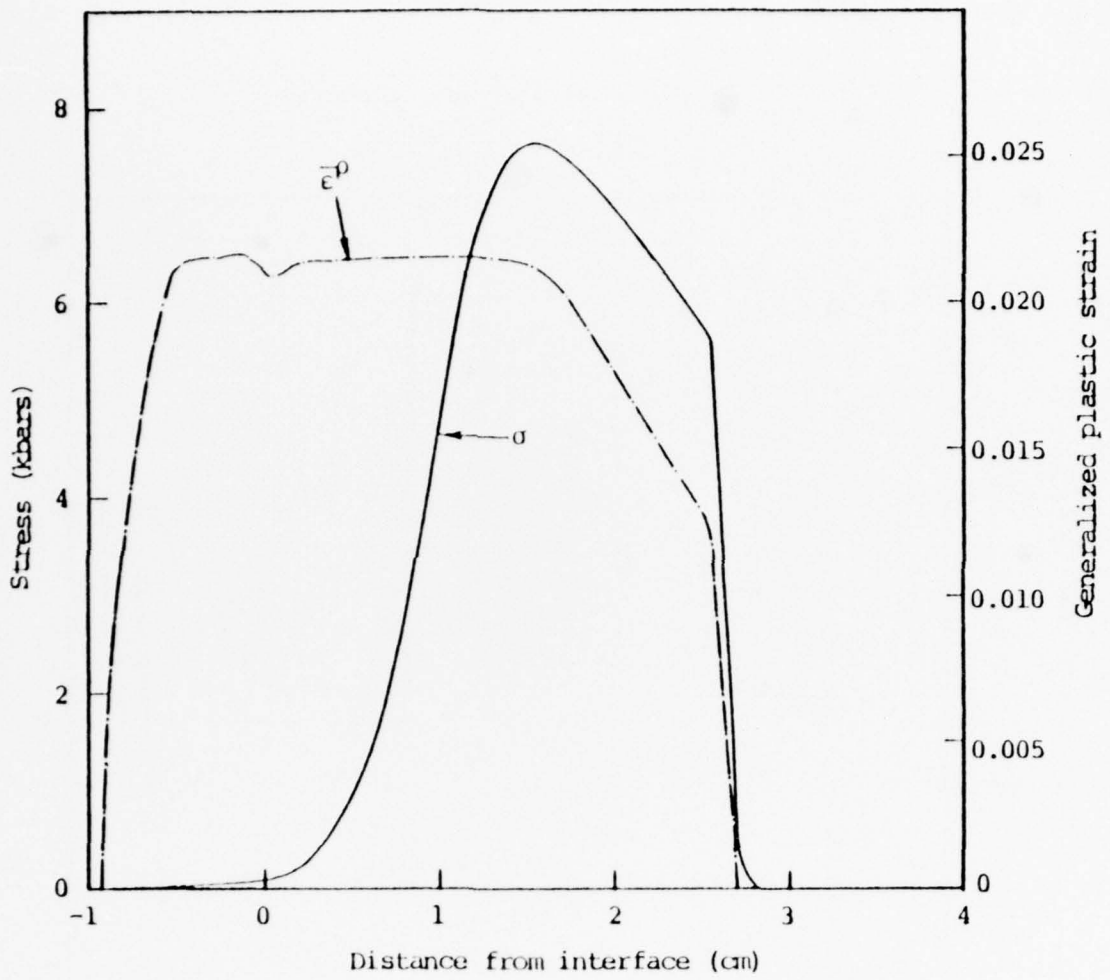

Figure 39. Stress and generalized plastic strain profiles at 10 μsec predicted by CAPRI code.

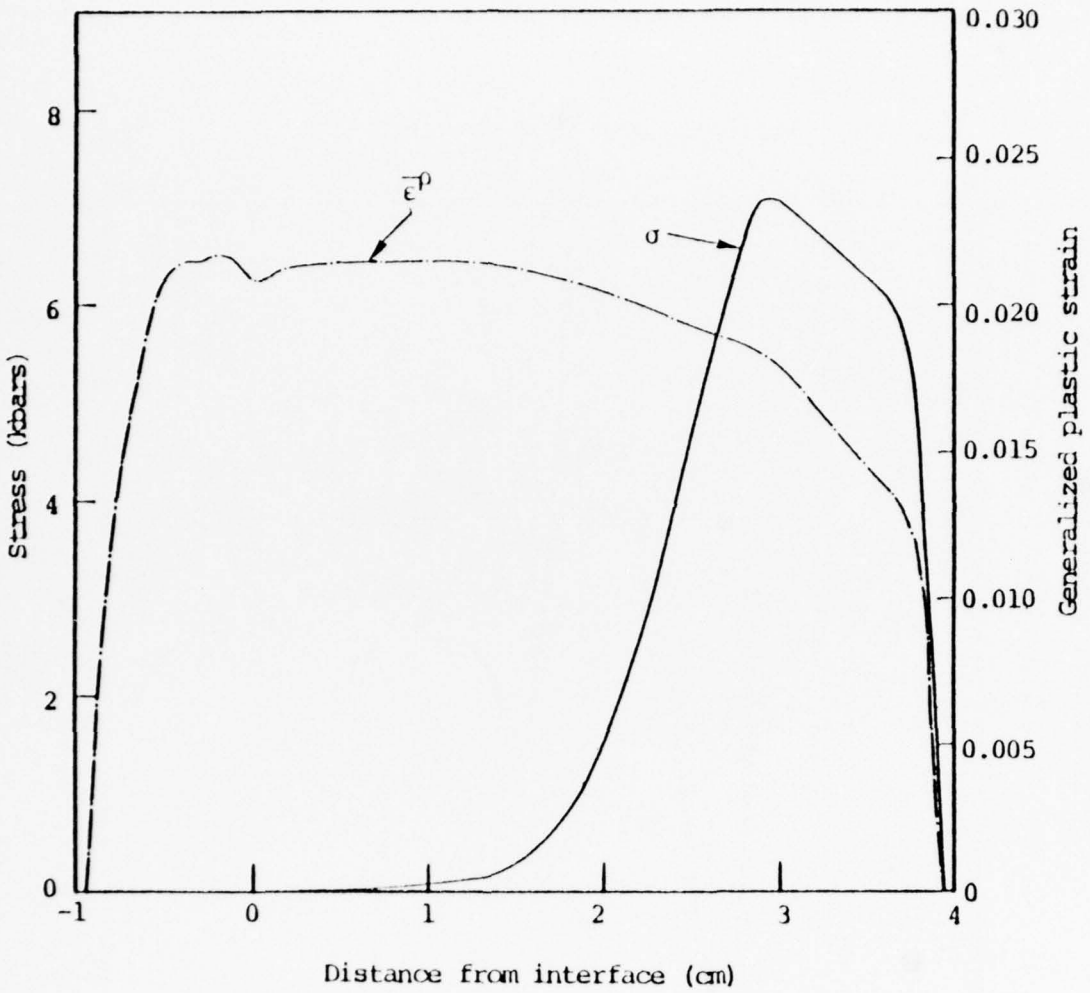

Figure 40. Stress and generalized plastic strain profiles at 15 μsec predicted by CAPRI code.

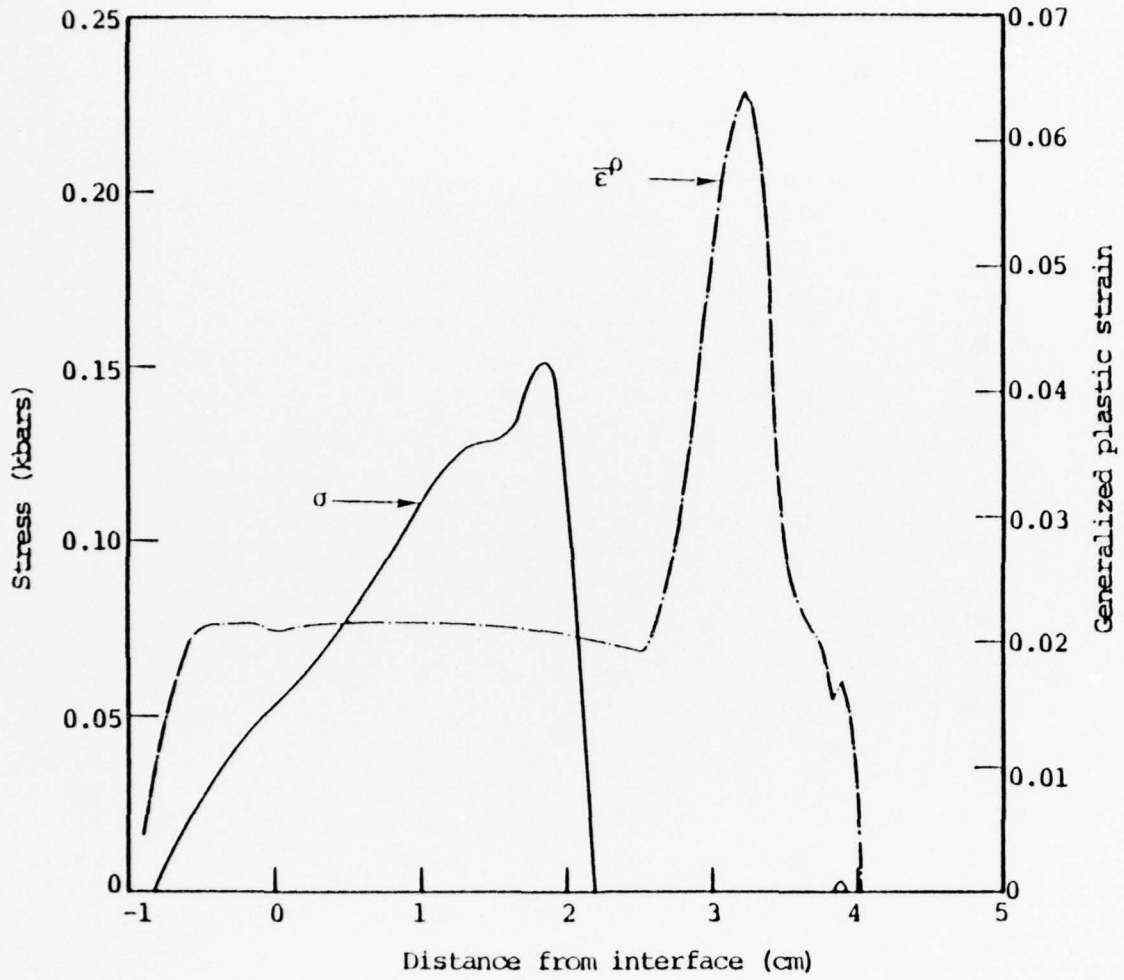

Figure 41. Stress and generalized plastic strain profile at 20 μsec predicted by CAPRI code.

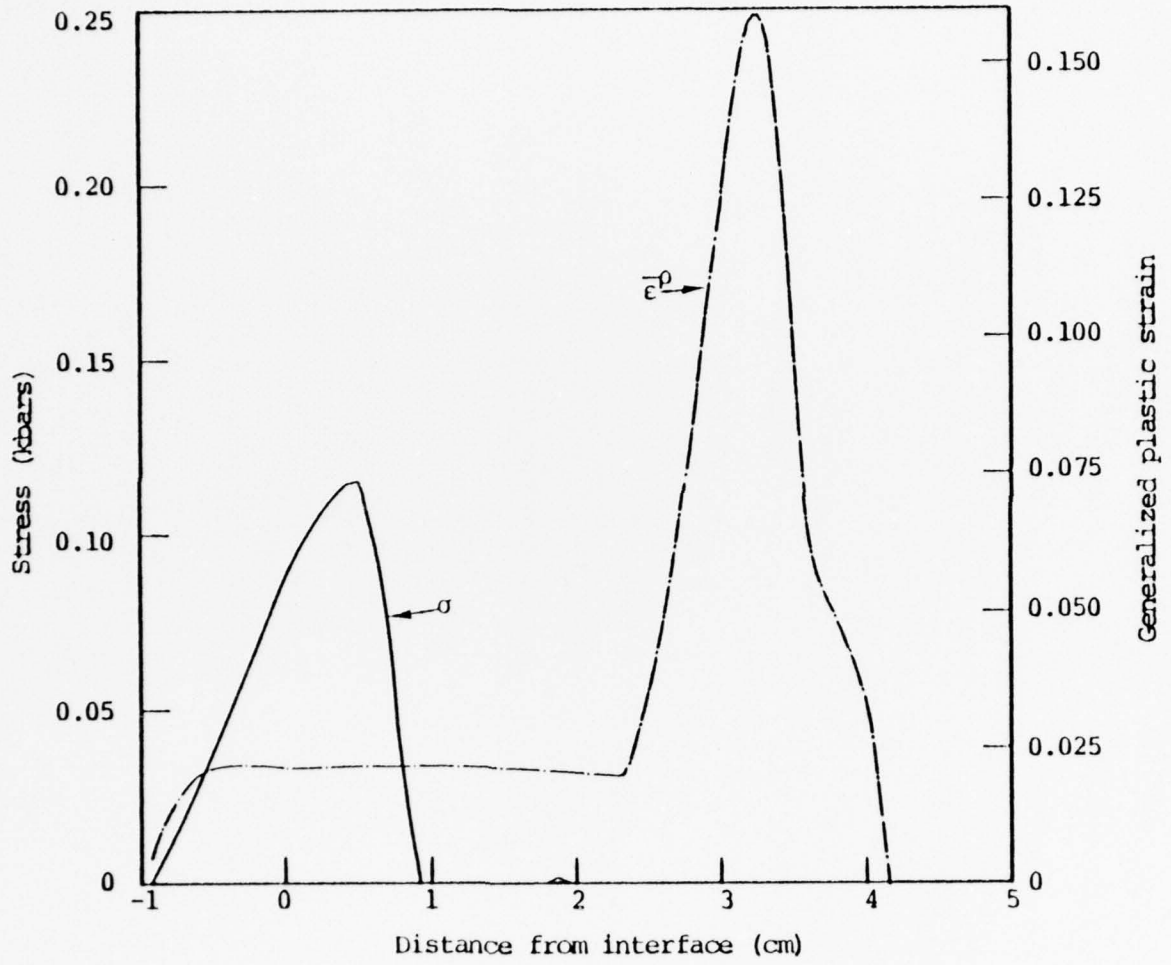

Figure 42. Stress and generalized plastic strain profiles at 25 μsec predicted by CAPRI code.

APPENDIX B

NUMERICAL ANALYSIS OF A SIMPLE PROBLEM INVOLVING FRICTIONAL SLIDING BETWEEN TWO SURFACES

The configuration of the problem considered in this section is depicted in Figure 43. Here, a cylindrical rod, initially at rest, is put in motion through sliding frictional contact with an annular region of like material moving with an initial axial velocity of V_o. As a result of the friction contact, the axial velocity of the rod, V_1, increases while that of the outer material, V_2, decreases. Eventually, the two materials reach the same axial velocity.

The materials are assumed to behave elastically with the bulk and shear moduli taken to have the respective values of 1,280 and 1,600 kbars. The initial density of the material was taken to be 7.8 gm/cm^3, while the frictional shearing stress τ_o between the sliding materials was assumed to have a constant value of 1.22 kbars. The inner material was initially at rest, while the outer material was given an initial velocity of 1.0×10^4 cm/sec.

B.1 THEORETICAL SOLUTION

A theoretical analysis of the motion of the two materials acted upon by a constant frictional shear stress, τ_o, at their common interface leads to the following expressions for the variation of the axial velocities V_1 and V_2 with time:

$$V_1 = \left(\frac{2\tau_o}{\rho r_1}\right) t \qquad \text{(B.1)}$$

$$V_2 = V_o - \left[\frac{2r_1\tau_o}{\rho(r_2^2 - r_1^2)}\right] t \qquad \text{(B.2)}$$

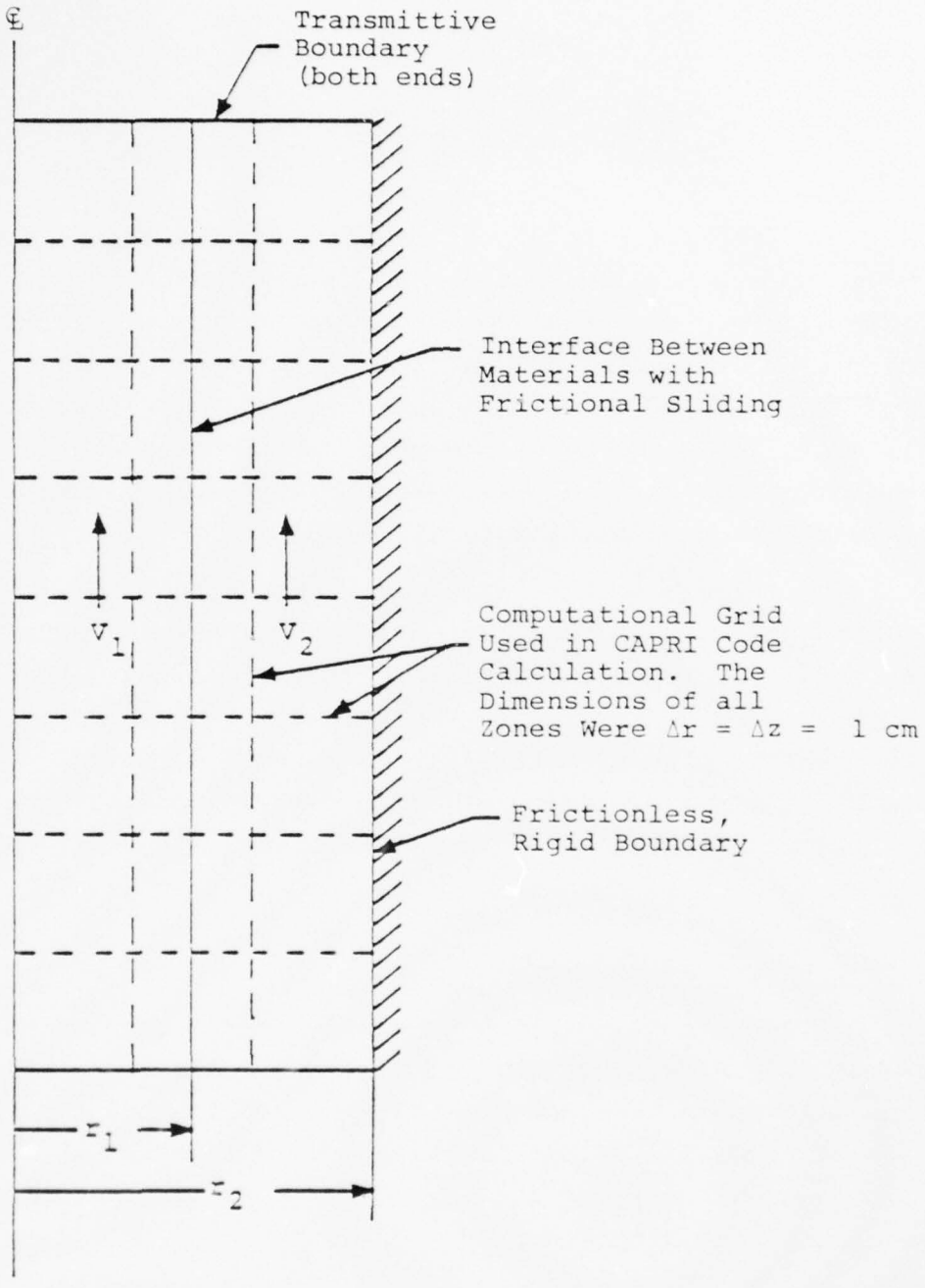

Figure 43. Configuration of problem considered to check out new sliding interface capability in CAPRI code.

where ρ is the density of the two materials, and r_1 and r_2 are defined in Figure 43. Furthermore, it can be shown that the two materials reach a common velocity of

$$V_c = V_o \left(1 - \frac{r_1^2}{r_2^2}\right) \tag{B.3}$$

at time, t_c, given by:

$$t_c = \left(\frac{\rho r_1}{2\tau_o}\right) V_c \tag{B.4}$$

B.2 NUMERICAL RESULTS

In the numerical solution to the problem depicted in Figure 43 a uniform Eulerian grid having zones with dimensions $\Delta r = \Delta z = 1$ cm was used. As indicated in Figure 43, three computational zones were used in the radial direction, with the (sliding) material interface passing midway through the interior zone. In the axial direction, eight zones were employed, and transmittive boundaries were used to introduce and remove material from both ends.

The CAPRI calculations were carried out to a time slightly less than that at which the two materials reached a common velocity. The results of the calculation are depicted in Figure 44, where the variation of the velocities V_1 and V_2 with time are shown. Also shown in this figure are the variations of V_1 and V_2 with time as given by the theoretical expressions in Equations B.1 and B.2. As an inspection of Figure 44 reveals, the agreement between the CAPRI code numerical results and the theoretical solution is extremely good for this relatively simple problem in which the sliding interface passes midway through the calculational cells and remains parallel to the vertical grid lines. Similar accuracy cannot, however, be expected for more complicated problems in which the sliding interface is not centrally positioned in the calculational grid.

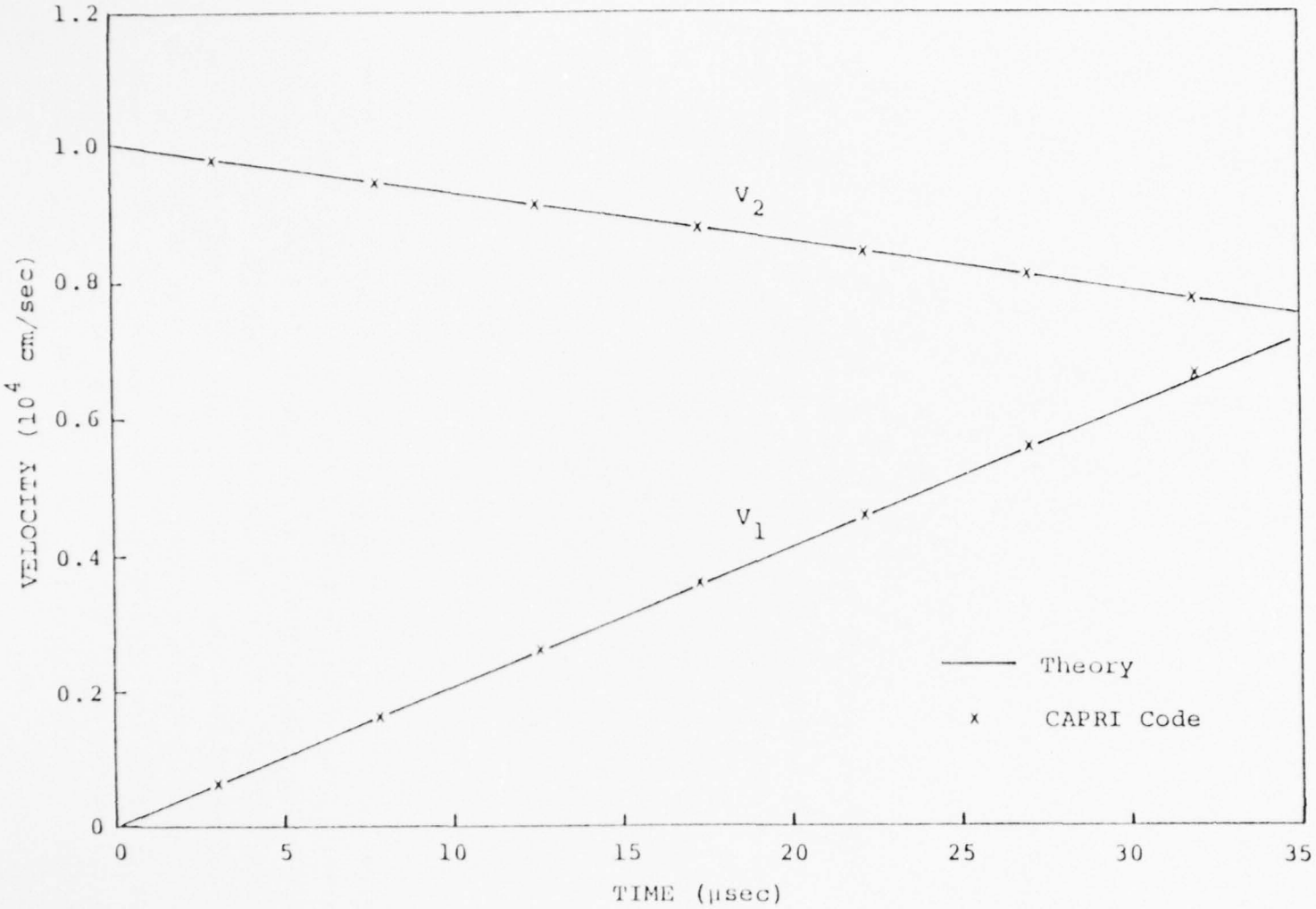

Figure 44. Variation of velocities V_1 and V_2 with time. Comparison between theoretical and CAPRI code numerical solutions.

DISTRIBUTION LIST

DEPARTMENT OF DEFENSE

Assistant to the Secretary of Defense
Atomic Energy
ATTN: Executive Assistant

Defense Advanced Rsch. Proj. Agency
ATTN: TIO

Defense Civil Preparedness Agency
ATTN: Hazard Eval. & Vul. Red. Div., G. Sisson

Defense Documentation Center
12 cy ATTN: DD

Defense Intelligence Agency
ATTN: DT-2
ATTN: DB-4C, E. O'Farrell
ATTN: RDS-3A
ATTN: DB-4E

Defense Nuclear Agency
ATTN: DDST
ATTN: SPAS
4 cy ATTN: TITL
5 cy ATTN: SPSS

Field Command
Defense Nuclear Agency
ATTN: FCPR

Field Command
Defense Nuclear Agency
ATTN: FCPRL

Interservice Nuclear Weapons School
ATTN: TTV

Joint Strat. Tgt. Planning Staff
ATTN: NRI-STINFO Library

NATO School (SHAPE)
ATTN: U.S. Documents Officer

Under Secy. of Def. for Rsch. & Engrg.
ATTN: Strategic & Space Systems (OS)

DEPARTMENT OF THE ARMY

Chief of Engineers
Department of the Army
2 cy ATTN: DAEN-MCE-D
2 cy ATTN: DAEN-RDM

Deputy Chief of Staff for Ops. & Plans
Department of the Army
ATTN: MOCA-ADL
ATTN: DAMO-NC

Deputy Chief of Staff for Rsch. Dev. & Acq.
Department of the Army
ATTN: DAMA-CSS-N, N. Barron

Engineer Studies Center
Department of the Army
ATTN: DAEN-FES

DEPARTMENT OF THE ARMY (Continued)

Gator Mine Program
Department of the Army
ATTN: E. Lindsey

Harry Diamond Laboratories
Department of the Army
ATTN: DELHD-N-P
ATTN: DELHD-N-P, J. Gwaltney

U.S. Army Armament Material Readiness Command
ATTN: MA, Library

U.S. Army Ballistic Research Labs.
ATTN: DRDAR-BLT, A. Ricchiazzi
ATTN: DRDAR-BLT, G. Roecker
ATTN: DRDAR-BLT, G. Grabarek
ATTN: DRDAR-BL
ATTN: DRDAR-BLT
ATTN: DRDAR-BLE, J. Keefer
2 cy ATTN: DRDAR-TSB-S

U.S. Army Cold Region Res. Engr. Lab.
ATTN: G. Swinzow

U.S. Army Comb. Arms Combat Dev. Acty.
ATTN: G. Steger
ATTN: LTC Pullen

U.S. Army Engineer Center
ATTN: ATZA

Division Engineer
U.S. Army Engineer Div., Huntsville
ATTN: HNDED-SR

U.S. Army Engineer Div., Missouri River
ATTN: Technical Library

U.S. Army Engineer School
ATTN: ATZA-DTE-ADM
ATTN: ATZA-CDC

U.S. Army Engr. Waterways Exper. Station
ATTN: G. Jackson
ATTN: D. Butler
ATTN: W. Flathau
ATTN: J. Strange
ATTN: L. Ingram
ATTN: Library
ATTN: B. Rohani
ATTN: P. Hadala

U.S. Army Mat. Cmd. Proj. Mngr. for Nuc. Munitions
ATTN: DRCPM-NUC

U.S. Army Material & Mechanics Rsch. Ctr.
ATTN: Technical Library

U.S. Army Materiel Dev. & Readiness Cmd.
ATTN: DRXAM-TL

U.S. Army Materiel Sys. Analysis Activity
ATTN: DRXSY-D, J. Sperrazza

DEPARTMENT OF THE ARMY (Continued)

U.S. Army Missile R&D Command
ATTN: W. Jann
ATTN: F. Fleming
ATTN: RSIC

U.S. Army Mobility Equip. R&D Cmd.
ATTN: DRDME-WC
ATTN: DRDDME-XS

U.S. Army Nuclear & Chemical Agency
ATTN: Library

U.S. Army War College
ATTN: Library

DEPARTMENT OF THE NAVY

Civil Engineering Laboratory
Naval Construction Battalion Center
ATTN: Code L51, R. Odello
ATTN: Code L08A

Marine Corps
Department of the Navy
ATTN: POM

Development Center
Fire Support Branch
Marine Corp Dev. & Education Command
Department of the Navy
ATTN: D091, J. Hartneady

Naval Air Systems Command
ATTN: F. Marquardt

Naval Explosive Ord. Disposal Fac.
ATTN: Code 504, J. Petrousky

Naval Facilities Engineering Command
ATTN: Code 09M22C

Naval Postgraduate School
ATTN: Code 0142, Library

Naval Research Laboratory
ATTN: Code 2627

Naval Sea Systems Command
ATTN: SEA-033
ATTN: SEA-9931G

Naval Surface Weapons Center
ATTN: Code X211
ATTN: Code F31
ATTN: Code U401, M. Kleinerman

Naval Surface Weapons Center
ATTN: Tech. Library & Info. Services Branch

Naval Weapons Center
ATTN: Code 266, C. Austin
ATTN: Code 233

Naval Weapons Evaluation Facility
ATTN: Code 10

Office of Naval Research
ATTN: Code 715

DEPARTMENT OF THE NAVY (Continued)

Office of the Chief of Naval Operations
ATTN: Code 604C3, R. Piacesi
ATTN: OP 982E42, M. Lenzini

Strategic Systems Project Office
Department of the Navy
ATTN: NSP-43

DEPARTMENT OF THE AIR FORCE

Air Force Armament Laboratory
ATTN: ADTC/XRS, M. Valentine
3 cy ATTN: DLYV, J. Collins

Air Force Institute of Technology
ATTN: Library

Air Force Weapons Laboratory, AFSC
ATTN: SUL

Assistant Chief of Staff
Intelligence
Department of the Air Force
ATTN: INT

Deputy Chief of Staff
Research, Development & Acq.
Department of the Air Force
ATTN: AFRDPX

Foreign Technology Division, AFSC
ATTN: NIIS Library

Oklahoma State University
Fld. Off. for Wpns. Effectiveness
Department of the Air Force
ATTN: F. Jackett

Rome Air Development Center, AFSC
ATTN: TSLD

Space & Missile Systems Organization
Air Force Systems Command
ATTN: RSS

DEPARTMENT OF ENERGY

Department of Energy
Albuquerque Operations Office
ATTN: CTID

Department of Energy
ATTN: Doc. Con. for Classified Library

Department of Energy
Nevada Operations Office
ATTN: Mail & Records for Technical Library

Department of Energy
ATTN: Doc. Con. for Research, Dev. and Test

OTHER GOVERNMENT AGENCIES

NASA
Ames Research Center
ATTN: R. Jackson

U.S. Nuclear Regulatory Commission
ATTN: Division of Security for L. Shao

DEPARTMENT OF ENERGY CONTRACTORS

Lawrence Livermore Laboratory
ATTN: L-504, M. Wilkins
ATTN: Technical Information Dept. Library
ATTN: J. Goubreau

Los Alamos Scientific Laboratory
ATTN: Report Library
ATTN: T. Dowler

Sandia Laboratories
ATTN: W. Altsmeirer
ATTN: W. Herrmann
ATTN: J. Calp
ATTN: W. Patterson
ATTN: J. Keisur
ATTN: 3141
ATTN: W. Caudle
ATTN: A. Chabai

Sandia Laboratories
ATTN: Library & Security Classification Div.

DEPARTMENT OF DEFENSE CONTRACTORS

Aerospace Corp.
ATTN: Technical Information Services

Agbabian Associates
ATTN: M. Agbabian

Applied Theory, Inc.
2 cy ATTN: J. Trulio

AVCO Research & Systems Group
ATTN: Library A830
ATTN: P. Grady
ATTN: D. Henderson

BCM Corp.
ATTN: Corporate Library

Boeing Co.
ATTN: Aerospace Library

California Research & Technology, Inc.
ATTN: K. Kreyenhagen
ATTN: Library

California Research & Technology, Inc.
ATTN: D. Orphal

Civil Systems Inc.
ATTN: J. Bratton

EG&G Washington Analytical Services Center, Inc.
ATTN: Library

Engineering Societies Library
ATTN: A. Mott

General Dynamics Corp.
ATTN: K. Anderson

General Electric Company-TEMPO
Center for Advanced Studies
ATTN: DASIAC

DEPARTMENT OF DEFENSE CONTRACTORS (Continued)

Georgia Institute of Technology
Georgia Tech. Research Institute
ATTN: L. Rehfield
ATTN: S. Hanagud

Honeywell, Inc.
Defense Systems Division
ATTN: T. Helvig

University of Illinois
Consulting Services
ATTN: N. Newmark
ATTN: W. Hall

Institute for Defense Analyses
ATTN: Classified Library

Kaman AviDyne
Division of Kaman Sciences Corp.
ATTN: Library
ATTN: N. Hobbs
ATTN: E. Criscione

Kaman Sciences Corp.
ATTN: Library

Lockheed Missiles & Space Co., Inc.
ATTN: M. Culp
ATTN: TIC-Library

Lockheed Missiles and Space Co., Inc.
ATTN: Technical Information Center

Martin Marietta Corp.
ATTN: H. McQuaig
ATTN: A. Cowan
ATTN: M. Anthony

Merritt CASES, Inc.
ATTN: J. Merritt
ATTN: Library

University of New Mexico
Dept. of Campus Security and Police
ATTN: G. Triandafalidis

Pacifica Technology
ATTN: G. Kent
ATTN: R. Bjork

Physics International Co.
ATTN: Technical Library
ATTN: L. Behrmann

R & D Associates
ATTN: P. Rausch
ATTN: A. Fields
ATTN: J. Lewis
ATTN: C. MacDonald
ATTN: H. Brode
ATTN: W. Wright, Jr.
ATTN: Technical Information Center

R & D Associates
ATTN: H. Cooper

Rand Corp.
ATTN: Library

DEPARTMENT OF DEFENSE CONTRACTORS (Continued)

Science Applications, Inc.
ATTN: Technical Library

SRI International
ATTN: G. Abrahamson
ATTN: J. Colton

Systems, Science & Software, Inc.
ATTN: Library
ATTN: R. Sedgewick
ATTN: H. Read
ATTN: J. Waddell
ATTN: E. Wilkins

Terra Tek, Inc.
ATTN: Library

DEPARTMENT OF DEFENSE CONTRACTORS (Continued)

TRW Defense & Space Sys. Group
ATTN: P. Dai
ATTN: Technical Information Center

TRW Defense & Space Sys. Group
ATTN: E. Wong

Weidlinger Assoc., Consulting Engineers
ATTN: M. Baron
ATTN: J. McCormick

Weidlinger Assoc., Consulting Engineers
ATTN: J. Isenberg